

# Measuring topological invariants for higher-order exceptional points in quantum three-mode systems

Pei-Rong Han<sup>1,2</sup>, Wen Ning<sup>1</sup>, Xin-Jie Huang<sup>1</sup>, Ri-Hua Zheng<sup>1</sup>, Shou-Bang Yang<sup>1</sup>, Fan Wu<sup>1</sup>, Zhen-Biao Yang<sup>1,3,\*</sup>, Qi-Ping Su<sup>4</sup>, Chui-Ping Yang<sup>4,†</sup> and Shi-Biao Zheng<sup>1,3,‡</sup>

<sup>1</sup>*Fujian Key Laboratory of Quantum Information and Quantum Optics,  
College of Physics and Information Engineering,  
Fuzhou University, Fuzhou, China*

<sup>2</sup>*School of Physics and Mechanical and Electrical Engineering,  
Longyan University, Longyan, China*

<sup>3</sup>*Hefei National Laboratory, Hefei, China*

<sup>4</sup>*School of Physics, Hangzhou Normal University, Hangzhou, China*

Owing to the presence of exceptional points (EPs), non-Hermitian (NH) systems can display intriguing topological phenomena without Hermitian analogs. However, experimental characterizations of exceptional topological invariants have been restricted to second-order EPs (EP2s) in classical or semiclassical systems. We here propose an NH multi-mode system with higher-order EPs, each of which is underlain by a multifold-degenerate multipartite entangled eigenstate. We implement the NH model by controllably coupling a Josephson-junction-based electronic mode to two microwave resonators. We experimentally quantify the topological invariant for an EP3, by mapping out the complex eigenspectra of the tripartite system along a loop surrounding this EP3 in the parameter space. The nonclassicality of the realized topology is manifested by the observed quantum correlations in the corresponding eigenstates. Our results extend research of exceptional topology to fully quantum-mechanical models with multipartite entangled eigenstates.

## I. INTRODUCTION

As one of the most well-tested physical theories, quantum mechanics has successfully passed numerous experimental tests. In most quantum-mechanical experiments, the system of interest is well isolated from its surrounding environment [1, 2], so that its dynamics is governed by the Schrödinger equation with an energy operator often called Hamiltonian. The Hermiticity of the Hamiltonian ensures that the system evolves unitarily. However, any real quantum system is inevitably coupled to the environment [3], which functions by entangling its degrees of freedom with the system state [4]. Through this entanglement, the environment continuously monitors the system state, which inevitably produces a measurement backaction [5]. Under this disturbance, the system dynamics could significantly deviate from the unitary evolution even when it does not make any quantum jump. Mathematically, the state trajectory, associated with this conditional evolution, is also governed by a Schrödinger equation but with a non-Hermitian (NH) Hamiltonian [6].

Due to the non-Hermiticity, two or more eigenvectors of the NH Hamiltonian can coalesce into a single one with the same eigenenergy at exceptional points (EPs) [7, 8]. These singularities can bring about many unique phenomena, exemplified by exotic topological phenomena that are absent in Hermitian systems [8–12]. The past two decades have witnessed a number of experimental explorations on the NH singular features, including spectral parity-time phase transitions [13–21], dynamical chiral behaviors [22–28], exceptional entanglement transitions [29], and NH topology [30–44]. The topological invariant of an NH system can be quantified in terms of the eigenvectors or the complex eigenenergies [8–12]. This is in distinct contrast with the Hermitian case, where the topology cannot be defined by the eigenenergies which are always real. So far, NH topology has been observed in several experiments, all of which were restricted to second-order EPs (EP2s) realized in classical systems [35–39] or with a classically-driven qubit [40–42]. Compared to EP2s, higher-order EPs can exhibit much richer topological properties [11, 12, 43–45] and the associated spectral topological invariants are defined in a fundamentally different manner [12]. Despite fundamental interest, such invariants have not been unambiguously characterized in experiment.

We here investigate both theoretically and experimentally the quantum-mechanical exceptional topology associated with higher-order EPs in an NH composite system consisting of multiple interacting modes. These EPs result from

\*E-mail: zbyang@fzu.edu.cn

†E-mail: yangcp@hznu.edu.cn

‡E-mail: t96034@fzu.edu.cn

continuous and nonunitary evolutions in the single-excitation subspace without quantum jumps [48]. The topological property associated to each higher-order EP can be quantified by the homotopy invariant, recently proposed by Delplace et al. [12]. We experimentally engineer the NH three-mode system in a superconducting circuit, where a nonlinear Xmon mode is controllably coupled to two photonic modes stored in two separated microwave resonators. The non-Hermiticity of the system is manifested by the non-negligible dissipation of one photonic mode. We find that the resulting NH Hamiltonian possesses four EP3s in the real parameter space. We quantify the homotopy invariant associated to the EP3 in the first quadrant of the parameter space, by mapping out the eigenenergies of the NH Hamiltonian along a loop surrounding this EP3. The system eigenenergies are extracted from the output states of the three-mode system in the single-excitation subspace, measured for different evolution times. As far as we know, this is the first experimental characterization of the topological invariant associated with a higher-order EP. We further note that the winding number defined by Eq. (3) is zero for the degenerate points in both the two-dimensional (2D) and 3D Hermitian systems, referred to as diabolical points (DPs), as well as for EP2s in a 2D NH system, as detailed in the Supplemental Material. Therefore, such a winding number serves as a homotopy invariant that uniquely characterizes the topology of EP3s.

## II. RESULTS

### A. NH multi-mode system

The system under consideration corresponds to a multi-mode system with competing coherent nearest-neighboring interactions and incoherent dissipation, as shown in Fig. 1a. Under the competition, the system evolution is a weighted mixture of infinitely many trajectories, among which of special interest is the one without quantum jump. This trajectory is governed by the NH Hamiltonian (setting  $\hbar = 1$ )

$$H_{\text{NH}} = -\frac{1}{2}i \sum_{j=1}^N \kappa_j a_j^\dagger a_j + \sum_{j=1}^{N-1} \lambda_j (a_j^\dagger a_{j+1} + \text{H.c.}), \quad (1)$$

where  $a_j^\dagger$  and  $a_j$  denote the creation and annihilation operators of the  $j$ th mode with a decaying rate  $\kappa_j$ ,  $\lambda_j$  represents the coupling coefficient between the  $j$ th and  $(j+1)$ th modes, and H.c. is the Hermitian conjugate. The excitation number of the total system is conserved along the no-jump trajectory, as the excitation number operator,  $N_e = \sum_{j=1}^N a_j^\dagger a_j$ , commutes with  $H_{\text{NH}}$ . Hereafter, we will consider the system behaviors restricted in the single-excitation subspace  $\{|1_1 0_2 \dots 0_N\rangle, \dots, |0_1 \dots 0_{N-1} 1_N\rangle\}$ , where  $|0_j\rangle$  and  $|1_j\rangle$  respectively denote the ground and first excited states for the  $j$ th mode with  $j$  ranging from 1 to  $N$ .

For  $\kappa_j = 0$  ( $j = 1, \dots, N$ ), the Hamiltonian (1) has  $N$  real eigenenergies, which display an  $N$ -fold degeneracy for  $\lambda_j = 0$ . When one or more modes are subjected to dissipations, the eigenenergies become complex. The resulting spectral structure can display exotic topological features without Hermitian analogues. To clearly illustrate the underlying NH quantum topological physics, we consider a three-mode system. For simplicity, we assume  $\kappa_2 = \kappa_3 = 0$ , and drop off the subscript of  $\kappa_1$ . Fig. 1b (c) shows the maximal real (imaginary) part of the gaps among the three complex eigenenergies versus  $\lambda_1$  and  $\lambda_2$ . The results clearly show that the non-Hermiticity splits the real degeneracy into four EP3s at  $\{\pm\lambda_1^c, \pm\lambda_2^c\}$  with  $\lambda_1^c = \sqrt{2}\kappa/3\sqrt{3}$  and  $\lambda_2^c = \kappa/6\sqrt{3}$ . At each EP3, the three eigenenergies have a vanishing real part and the same nonzero imaginary part.

The spectrum of the NH Hamiltonian exhibits a rich structure, where each of the four EP3s is connected to two curves of EP2s (solid lines in Fig. 1d), at which a pair of eigenstates and eigenenergies coalesce. The details of these eigenenergies are shown in Sec. S5 of the Supplemental Material. Enclosed in the EP2 contour is an isofrequency region, where all the three eigenenergies have the same real part. This is a 2D generalization of the linear-like two-fold degenerate Fermi arc, which connects 2 EP2s existing in a 2D system [30]. In the isofrequency region, the real parts of the three complex eigenenergies vanish, so that the state evolution of the system is determined by the imaginary parts of these eigenenergies, each of which corresponds to a gaining or losing rate depending upon its sign. After a long-time evolution, only the eigenvector with the largest imaginary part can survive for the no-jump case. Since such an eigenvector is essentially a tripartite entangled state, the dynamics in the isofrequency region provides a way for robust generation and conditional stabilization of tripartite entanglement [49]. Such an entanglement generation and stabilization process is illustrated by the simulations presented in Sec. S2 of the Supplemental Material.

In addition to the real Fermi arc, each of the four EP3s emanates an i-Fermi arc (dashed lines in Fig. 1d) [11], along which the imaginary parts are three-fold degenerate. With a global shift of the spectrum by a suitable imaginary value, the four i-Fermi arcs correspond to the regions where the eigenenergies are all real. In view of spectral phase transitions, each of the four EP3s corresponds to a tripoint, where three distinct phases (featuring imaginary, real, and complex energy gaps) meet together.

## B. Experimental implementation

We perform the experiment using a circuit quantum electrodynamics device with five nonlinear Xmon modes (qubits), each controllably coupled to the common bus resonator ( $R_b$ ) of a fixed frequency  $\omega_b/2\pi = 5.58$  GHz. The NH quantum multipartite system is realized with one of these qubits (labeled as  $Q$ ), the bus resonator  $R_b$ , and the readout resonator of  $Q$ , ( $R_r$ ), which has a frequency  $\omega_r/2\pi = 6.66$  GHz. The on-resonance coupling strength between  $Q$  and  $R_b$  ( $R_r$ ) is  $g_b = 2\pi \times 20$  MHz ( $g_r = 2\pi \times 41$  MHz). The decaying rate of  $Q$  ( $R_b$ ) is 0.06 (0.08) MHz, which is two orders smaller than that of  $R_r$  ( $\kappa = 5$  MHz). Thus, the dissipations of  $Q$  and  $R_b$  are negligible. To realize the NH tripartite Hamiltonian in a controllable manner, two parametric modulations are simultaneously applied to  $Q$  to modulate its transition frequency as  $\omega_q = \omega_0 + \sum_{j=1,2} \varepsilon_j \cos(\nu_j t)$ , where  $\omega_0$  is the mean frequency of  $Q$ , and  $\varepsilon_j$  and  $\nu_j$  respectively denote the amplitude and frequency of the  $j$ th modulation, as depicted in Fig. 2a. Under the condition  $\omega_0 + \nu_1 = \omega_r$ , the qubit  $Q$  interacts with the readout resonator  $R_r$  at the first upper sideband for the first modulation, with the strength  $\lambda_1 = g_r J_1(\varepsilon_1/\nu_1)$ . Here,  $J_1(\mu)$  is the first-order Bessel function of the first kind. The second modulation is used to induce the sideband interaction between  $Q$  and  $R_b$ , with the effective photonic swapping rate  $\lambda_2$  controlled by  $\varepsilon_2$ . The sideband interactions and the system parameters are detailed in Sec. S3 of the Supplemental Material. When the  $R_r$ - $Q$ - $R_b$  system initially has one excitation, its dynamics, associated with no-jump trajectory, is described by the NH Hamiltonian (1) with  $N = 3$ , where  $R_r$ ,  $Q$ , and  $R_b$  correspond to three modes sharing a single excitation.

The experiment starts with the preparation of an initial single-excitation state, following which the parametric modulations are applied to  $Q$ , with the experimental pulse sequence depicted in Fig. 2b. After a preset interaction time  $t$ , the parametric modulations are switched off to have  $Q$  decoupled from both  $R_b$  and  $R_r$ . The output state of the system, associated with the no-jump trajectory, is given by

$$|\psi(t)\rangle = c_1(t) |0_r 0_q 1_b\rangle + c_2(t) |0_r 1_q 0_b\rangle + c_3(t) |1_r 0_q 0_b\rangle. \quad (2)$$

Here the subscripts  $r$ ,  $q$ , and  $b$  label  $R_r$ ,  $Q$ , and  $R_b$ , respectively. As the excitation is conserved by the NH Hamiltonian while the quantum jump breaks down this conservation, the no-jump state trajectory can be postselected by discarding the outcome with null excitation. The joint tripartite output state is read out with the assistance of two ancilla qubits, denoted as  $Q_1$  and  $Q_2$ . The  $R_r$ - $Q$ - $R_b$  output state is mapped to the  $Q$ - $Q_2$ - $Q_1$  system, which is realized by swapping gates (see Sec. S4 in the Supplemental Material). Bloch vectors of the three qubits along different axes are then measured. By correlating the outcomes of these measurements, the three-qubit density matrix is reconstructed. Removing the ground state element and renormalizing the remaining ones, we obtain the final state of the system evolving under the NH Hamiltonian. With a correction for the infidelity of the state mapping, the resulting  $Q$ - $Q_2$ - $Q_1$  output state corresponds to the  $R_r$ - $Q$ - $R_b$  output state right before the state mapping. Fig. 2c shows the evolution of the populations  $|0_r 0_q 1_b\rangle$ ,  $|0_r 1_q 0_b\rangle$ , and  $|1_r 0_q 0_b\rangle$  for the initial state  $|0_r 1_q 0_b\rangle$ , measured at the point  $\lambda_1 = 2\pi \times 0.21$  MHz and  $\lambda_2 = 2\pi \times 0.31$  MHz. These populations are obtained by discarding the measurement outcome  $|0_r 0_q 0_b\rangle$  and then renormalizing the probabilities for occurrences of the three single-excitation outcomes.

## C. Measurement of the winding number

The topological invariant associated with each EP3 can be quantified by the winding number, calculated in terms of the resultant vector  $\mathcal{R}$  [12]

$$\mathcal{W} = \frac{1}{2\pi} \sum_{j=1,2} \oint_{C_\lambda} \frac{1}{\|\mathcal{R}\|^2} \left( \mathcal{R}_1 \frac{\partial \mathcal{R}_2}{\partial \lambda_j} - \mathcal{R}_2 \frac{\partial \mathcal{R}_1}{\partial \lambda_j} \right) d\lambda_j, \quad (3)$$

where the integral loop  $C_\lambda$  encloses the EP3 in the 2D parameter space.  $\mathcal{R}_1$  and  $\mathcal{R}_2$  depend upon the eigenenergies (for details, see Sec. S7 in the Supplemental Material), which can in principle be extracted from the output states measured for different interaction times. To simplify the measurement, we choose a square-shaped loop on the  $\lambda_1$ - $\lambda_2$  plane. The loop has four vertices  $(0, 0)$ ,  $(\lambda_m, 0)$ ,  $(0, \lambda_m)$ , and  $(\lambda_m, \lambda_m)$ , as shown in Fig. 3a. With this choice, the eigenspectrum can be extracted in a relatively easy manner (see Sec. S5 in the Supplemental Material). In our experiment,  $\lambda_m$  is set to be  $2\pi \times 1$  MHz.

The eigenenergies, measured along the four edges of the square-shaped loop, are detailed in Sec. S8 of the Supplemental Material. For different values of  $\lambda_1$  or  $\lambda_2$ ,  $\mathcal{R}_1$ , and  $\mathcal{R}_2$  are calculated from the corresponding measured eigenenergies, as shown in Fig. 3b-e. The dashed lines denote the functions fitted with the measured data. We note that the rescaled unit resultant vector, defined as  $\mathcal{R}^u = (\mathcal{R}_1 + i\mathcal{R}_2)/|\mathcal{R}|$ , is changed along a circle when the control parameter  $(\lambda_1, \lambda_2)$  is varied along a loop enclosing the EP3, as illustrated in Fig. 3f. On the edge with  $\lambda_2 = 0$ , there

is an EP2, within the vicinity of which the resultant vector undergoes a  $\pi$  rotation, as detailed in the insets of Fig. 3b. This rotation occurs in a very narrow region of the control parameter  $(\lambda_1, \lambda_2)$ , but contributes half of the circular trajectory of  $\mathcal{R}^u$ . The winding number based on thus-obtained  $\mathcal{R}_1$  and  $\mathcal{R}_2$  is  $\mathcal{W} = 1$ , which confirms that the loop encircles an EP3. In addition to the EP3, the loop surrounds infinitely multiple EP2s, which form two exceptional arcs that cross at the EP3, as illustrated in Fig. 3a. These EP2s have no contribution to the characterized topological invariant, which corresponds to the winding number of the relative angle between  $\mathcal{R}_1$  and  $\mathcal{R}_2$  [12]. This implies that the spectral topological features of higher EPs are fundamentally distinct from those of EP2s. As detailed in Ref. [12], the winding number defined in Eq. (3) is the simplest example of the homotopy invariants, which can quantify topological properties of multifold symmetry-protected EPs but have not been experimentally characterized so far.

In a recent acoustic experiment [43], the measured local phase rigidities of the eigenvectors near an EP3 have a critical exponent coinciding with the winding number quantifying the calculated global Berry phase. However, the Berry phase itself, which characterizes the topological charge associated to the eigenvectors, has not been experimentally extracted, neither has the eigenspectral topological invariant. In a recent experiment [47], a third-order exceptional line was observed with a nitrogen-vacancy system, where the NH Hamiltonian for a single electron with three levels was constructed by the dilation method. However, the topological properties of the realized EP3 have not been experimentally characterized. As far as we know, our work represents the first measurement of homotopy invariants, of which the winding number for EP3s is the simplest example [12].

To reveal the quantum correlations among the three modes, we perform quantum state tomography on the output state of the system. For different values of the control parameters, the evolutions of the measured pairwise concurrences are detailed in Sec. S5 of the Supplemental Material. For the edges  $\lambda_1 = 0$  and  $\lambda_2 = 0$ , the system reduces to a two-mode system, so that the eigenstates can be extracted from the state evolution in a relatively easy way. At point  $(0, \lambda_m)$ , the measured concurrences of the two eigenstates ( $|\Phi_{\pm}\rangle$ ) for the  $R_b$ - $Q$  subsystem, which is decoupled from  $R_r$ , are 0.997 and 0.997, respectively. At point  $(\lambda_m, 0)$ , the concurrences for two measured  $Q$ - $R_r$  eigenstates ( $|\Phi'_{\pm}\rangle$ ) are respectively 0.971 and 0.971. When  $\lambda_1 \neq 0$  and  $\lambda_2 \neq 0$ , each of the three eigenstates corresponds to a tripartite entangled eigenstate, for which each mode is quantum-mechanically correlated to either of the other two modes. Experimental extraction of these eigenstates is a challenging task because each eigenstate involves four parameters to be determined. However, the observation of tripartite entangled states, evolved from the initial product state  $|0_b 1_q 0_r\rangle$ , indicates that there exists tripartite entanglement in the underlying eigenstates. These observed nonclassical correlations represent another unique feature that fundamentally distinguishes the presently observed topology from those previously demonstrated in classical or semiclassical systems [30–45].

### III. DISCUSSION

In conclusion, we have investigated the exceptional topology in interacting many-body quantum systems, with a competition between coherent couplings and incoherent dissipation. The quantum topology is manifested by the presence of multiple higher-order EPs, each of which carries a quantized topological charge and is associated with a multi-fold degenerate eigenstate displaying highly nonclassical correlations. The NH model is experimentally realized with a superconducting qubit, which is correlated to a lossless bus resonator and a decaying readout resonator by swapping a single photon. The topological charge at each EP3 is quantified by the winding number, extracted from the eigenspectra measured with the assistance of two ancilla qubits. Each of the corresponding eigenstates exhibits quantum entanglement, confirming the nonclassical origin of the topology. Besides fundamental interest, the demonstrated NH dynamics associated with higher order EPs may have applications in quantum technologies, such as sensitivity enhancement in quantum metrology [50] as well as fast and robust generation of quantum entanglement [51].

### IV. DATA AVAILABILITY

The data that support the findings of this study are available from the corresponding author upon request.

- 
- [1] Wineland, D. J. Nobel Lecture: Superposition, entanglement, and raising Schrödinger's cat. *Rev. Mod. Phys.* **85**, 1103–1114 (2013).
  - [2] Haroche, S. Nobel Lecture: Controlling photons in a box and exploring the quantum to classical boundary. *Rev. Mod. Phys.* **85**, 1083–1102 (2013).



- [3] Scully, M. O. & Zubairy, M. S. Quantum Optics (Cambridge, 2000).
- [4] Zurek, W. H. Decoherence, einselection, and the quantum origins of the classical. *Rev. Mod. Phys.* **75**, 715–775 (2003).
- [5] Ashida, Y., Gong, Z. & Ueda, M. Non-Hermitian physics. *Adv. Phys.* **69**, 249–435 (2020).
- [6] Bender, C. M. & Boettcher, S. Real spectra in non-Hermitian Hamiltonians having  $\mathcal{PT}$  symmetry. *Phys. Rev. Lett.* **80**, 5243–5246 (1998).
- [7] Özdemir, Ş. K., Rotter, S., Nori, F. & Yang, L. Parity-time symmetry and exceptional points in photonics. *Nat. Mater.* **18**, 783–798 (2019).
- [8] Ding, K., Fang, C. & Ma, G. Non-Hermitian topology and exceptional-point geometries. *Nat. Rev. Phys.* **4**, 745–760 (2022).
- [9] Bergholtz, E. J., Budich, J. C. & Kunst, F. K. Exceptional topology of non-Hermitian systems. *Rev. Mod. Phys.* **93**, 015005 (2021).
- [10] Gong, Z., Ashida, Y., Kawabata, K., Takasan, K., Higashikawa, S. & Ueda, M. Topological phases of non-Hermitian systems. *Phys. Rev. X* **8**, 031079 (2018).
- [11] Mandal, I. & Bergholtz, E. J. Symmetry and higher-order exceptional points. *Phys. Rev. Lett.* **127**, 186601 (2021).
- [12] Delplace, P., Yoshida, T. & Hatsugai, Y. Symmetry-protected multifold exceptional points and their topological characterization. *Phys. Rev. Lett.* **127**, 186602 (2021).
- [13] Choi, Y., Kang, S., Lim, S., Kim, W., Kim, J.-R., Lee, J.-H. & An, K. Quasieigenstate coalescence in an atom-cavity quantum composite. *Phys. Rev. Lett.* **104**, 153601 (2010).
- [14] Xiao, L., Wang, K., Zhan, X., Bian, Z., Kawabata, K., Ueda, M., Yi, W. & Xue, P. Observation of critical phenomena in parity-time-symmetric quantum dynamics. *Phys. Rev. Lett.* **123**, 230401 (2019).
- [15] Öztürk, F. E., Lappe, T., Hellmann, G., Schmitt, J., Klaers J. & Vewinger, F. Observation of a non-Hermitian phase transition in an optical quantum gas. *Science* **372**, 88–91 (2021).
- [16] Peng, P., Cao, W., Shen, C., Qu, W., Wen, J., Jiang, L. & Xiao, Y. Anti-parity-time symmetry with flying atoms. *Nat. Phys.* **12**, 1139–1145 (2016).
- [17] Li, J., Harter, A. K., Liu, J., Melo, L. d., Joglekar, Y. N. & Luo, L. Observation of parity-time symmetry breaking transitions in a dissipative Floquet system of ultracold atoms. *Nat. Commun.* **10**, 855 (2019).
- [18] Wu, Y., Liu, W., Geng, J., Song, X., Ye, X., Duan, C.-K., Rong, X. & Du, J. Observation of parity-time symmetry breaking in a single-spin system. *Science* **364**, 878–880 (2019).
- [19] Naghiloo, M., Abbasi, M., Joglekar, Y. N. & Murch, K. W. Quantum state tomography across the exceptional point in a single dissipative qubit. *Nat. Phys.* **15**, 1232–1236 (2019).
- [20] Wang, Z., Xiang, Z., Liu, T., Song, X., Song, P., Guo, X., Su, L., Zhang, H., Du, Y. & Zheng, D. Observation of the exceptional point in superconducting qubit with dissipation controlled by parametric modulation. *Chin. Phys. B* **30**, 100309 (2021).
- [21] Gao, T. *et al.* Observation of non-Hermitian degeneracies in a chaotic exciton-polariton billiard. *Nature (London)* **526**, 554–558 (2015).
- [22] Zhang, X.-L., Wang, S., Hou, B. & Chan, C. T. Dynamically encircling exceptional points: In situ control of encircling loops and the role of the starting point. *Phys. Rev. X* **8**, 021066 (2018).
- [23] Doppler, J., Mailybaev, A. A., Böhm, J., Kuhl, U., Girschik, A., Libisch, F., Milburn, T. J., Rabl, P., Moiseyev, N. & Rotter, S. Dynamically encircling an exceptional point for asymmetric mode switching. *Nature (London)* **537**, 76–79 (2016).
- [24] Xu, H., Mason, D., Jiang, L. & Harris, J. G. E. Topological energy transfer in an optomechanical system with exceptional points. *Nature (London)* **537**, 80–83 (2016).
- [25] Yoon, J. W. *et al.* Time-asymmetric loop around an exceptional point over the full optical communication band. *Nature (London)* **562**, 86–90 (2018).
- [26] Liu, W., Wu, Y., Duan, C.-K., Rong, X. & Du, J. Dynamically encircling an exceptional point in a real quantum system. *Phys. Rev. Lett.* **126**, 170506 (2021).
- [27] Gou, W., Chen, T., Xie, D., Xiao, T., Deng, T.-S., Gadway, B., Yi, W. & Yan, B. Tunable nonreciprocal quantum transport through a dissipative Aharonov-Bohm ring in ultracold atoms. *Phys. Rev. Lett.* **124**, 070402 (2020).
- [28] Ren, Z., Liu, D., Zhao, E., He, C., Pak, K. K., Li, J. & Jo, G.-B. Chiral control of quantum states in non-Hermitian spin-orbit-coupled fermions. *Nat. Phys.* **18**, 385–389 (2022).
- [29] Han, P. R., Wu, F., Huang, X. J., Wu, H. Z., Zou, C. L., Yi, W., Zhang, M., Li, H., Xu, K., Zheng, D., Fan, H., Wen, J., Yang, Z. B. & Zheng, S. B. Exceptional entanglement phenomena: Non-Hermiticity meeting non-classicality. *Phys. Rev. Lett.* **131**, 260201 (2023).
- [30] Dembowski, C., Gräf, H.-D., Harney, H. L., Heine, A., Heiss, W. D., Rehfeld, H. & Richter, A. Experimental observation of the topological structure of exceptional points. *Phys. Rev. Lett.* **86**, 787–790 (2001).
- [31] Zhou, H., Peng, C., Yoon, Y., Hsu, C. W., Nelson, K. A., Fu, L., Joannopoulos, J. D., Soljačić, M. & Zhen, B. Observation of bulk Fermi arc and polarization half charge from paired exceptional points. *Science* **359**, 1009–1012 (2018).
- [32] Cerjan, A., Huang, S., Wang, M., Chen, K. P., Chong, Y. & Rechtsman, M. C. Experimental realization of a Weyl exceptional ring. *Nat. Photon.* **13**, 623–628 (2019).
- [33] Liu, J. J., Li, Z. W., Chen, Z. G., Tang, W., Chen, A., Liang, B., Ma, G. & Cheng, J.-C. Experimental realization of Weyl exceptional rings in a synthetic three-dimensional non-Hermitian phononic crystal. *Phys. Rev. Lett.* **129**, 084301 (2022).
- [34] Zhen, B., Hsu, C. W., Igarashi, Y., Lu, L., Kaminerv, Pick, A., Chua, S.-L., Joannopoulos, J. D. & Soljačić, M. Spawning rings of exceptional points out of Dirac cones. *Nature (London)* **525**, 354–358 (2015).
- [35] Wang, K., Dutt, A., Yang, K. Y., Wojcik, C. C., Vučković, J. & Fan, S. Generating arbitrary topological windings of a

- non-Hermitian band. *Science* **371**, 1240–1245 (2021).
- [36] Wang, K., Dutt, A., Wojcik, C. C. & Fan, S. Topological complex-energy braiding of non-Hermitian bands. *Nature (London)* **598**, 59–64 (2021).
  - [37] Zhang, Q., Li, Y., Sun, H., Liu, X., Zhao, L., Feng, X., Fan, X. & Qiu, C. Observation of acoustic non-Hermitian Bloch braids and associated topological phase transitions. *Phys. Rev. Lett.* **130**, 017201 (2023).
  - [38] Tang, W., Ding, K. & Ma, G. Direct measurement of topological properties of an exceptional parabola. *Phys. Rev. Lett.* **127**, 034301 (2021).
  - [39] Su, R. *et al.* Direct measurement of a non-Hermitian topological invariant in a hybrid light-matter system. *Sci. Adv.* **7**, eabj8905 (2021).
  - [40] Zhang, W., Ouyang, X., Huang, X., Wang, X., Zhang, H., Yu, Y., Chang, X., Liu, Y., Deng, D.-L. & Duan, L.-M. Observation of non-Hermitian topology with nonunitary dynamics of solid-state spins. *Phys. Rev. Lett.* **127**, 090501 (2021).
  - [41] Cao, M.-M., Li, K., Zhao, W.-D., Guo, W.-X., Qi, B.-X., Chang, X.-Y., Zhou, Z.-C., Xu, Y. & Duan, L.-M. Probing complex-energy topology via non-Hermitian absorption spectroscopy in a trapped ion simulator. *Phys. Rev. Lett.* **130**, 163001 (2023).
  - [42] Wu, Y., Wang, Y., Ye, X., Liu, W., Duan, C.-K., Wang, Y., Rong, X. & Du, J. Observation of the knot topology of non-Hermitian systems in a single spin. *Phys. Rev. A* **108**, 052409 (2023).
  - [43] Tang, W., Jiang, X., Ding, K., Xiao, Y.-X., Zhang, Z.-Q., Chan, C. T. & Ma, G. Exceptional nexus with a hybrid topological invariant. *Science* **370**, 1077–1080 (2020).
  - [44] Tang, W., Ding, K. & Ma, G. Realization and topological properties of third-order exceptional lines embedded in exceptional surfaces. *Nat. Commun.* **14**, 6660 (2023).
  - [45] Patil, Y. S. S., Höller, J., Henry, P. A., Guria, C., Zhang, Y., Jiang, L., Kralj, N., Read, N. & Harris, J. G. E. Measuring the knot of non-Hermitian degeneracies and non-commuting braids. *Nature (London)* **607**, 271–275 (2022).
  - [46] Lin, Q., Yi, W. & Xue, P. Manipulating directional flow in a two-dimensional photonic quantum walk under a synthetic magnetic field. *Nat. Commun.* **14**, 6283 (2023).
  - [47] Wu, Y., Wang, Y., Ye, X., Liu, W., Niu, Z., Duan, C. K., Wang, Y., Rong, X. & Du, J. Third-order exceptional line in a nitrogen-vacancy spin system. *Nat. Nanotechnol.* **19**, 160–165 (2024).
  - [48] Minganti, F., Miranowicz, A., Chhajlany, R. W. & Nori, F. Quantum exceptional points of non-Hermitian Hamiltonians and Liouvillians: The effects of quantum jumps. *Phys. Rev. A* **100**, 062131 (2019).
  - [49] Teixeira, W. S., Vadimov, V., Mörstedt, T., Kund, S. & Möttönen, M. Exceptional-point-assisted entanglement, squeezing, and reset in a chain of three superconducting resonators. *Phys. Rev. Res.* **5**, 033119 (2023).
  - [50] Chen, W., Özdemir, Ş. K., Zhao, G., Wiersig, J. & Yang, L. Exceptional points enhance sensing in an optical microcavity. *Nature (London)* **548**, 192–196 (2017).
  - [51] Li, Z.-Z., Chen, W., Abbasi, M., Murch, K. W. & Whaley, K. B. Speeding up entanglement generation by proximity to higher-order exceptional points. *Phys. Rev. Lett.* **131**, 100202 (2023).

## V. ACKNOWLEDGEMENTS

S. B. Zheng was supported by the National Natural Science Foundation of China (Grant Nos. 12274080, 12474356) and the Innovation Program for Quantum Science and Technology (Grant No. 2021ZD0300200); Z. B. Yang was supported by the National Natural Science Foundation of China (Grant No. 12475015) and the Innovation Program for Quantum Science and Technology (Grant Nos. 2021ZD0300200); C. P. Yang was supported by the National Natural Science Foundation of China (Grant No. U21A20436) and the Innovation Program for Quantum Science and Technology (Grant Nos. 2021ZD0301705).

## VI. AUTHOR CONTRIBUTIONS

S.-B.Z. proposed the theoretical model and conceived the experiment. P.-R.H., W.N., X.-J.H. supervised by Z.-B.Y. and S.-B.Z., carried out the experiment. P.-R.H., R.-H.Z, S.-B.Y, F.W., Q.-P.S, C.-P.Y., and S.-B.Z. analyzed the data. S.-B.Z., Z.-B.Y., and C.-P.Y. cowrote the paper. All authors contributed to interpretation of observed phenomena, and helped to write the paper.

## VII. COMPETING INTERESTS

The authors declare no competing interests.

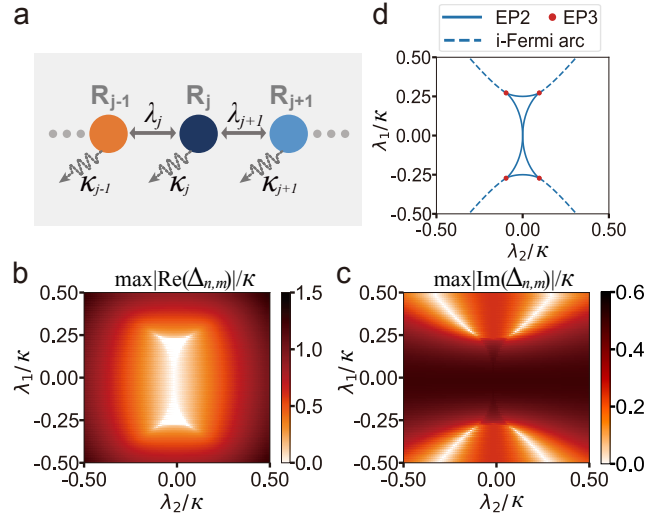


FIG. 1: Sketch of the NH multimode system and the spectral structure. (a) Theoretical model. The system involves  $N$  modes ( $R_j$ ), arranged in a linear array. The NH Hamiltonian dynamics features the competition between the nearest-neighbor swapping couplings ( $\lambda_j$ ) and the energy dissipations ( $\kappa_j$ ). (b), (c) Maxima for the real (b) and imaginary (c) gaps versus  $\lambda_1$  and  $\lambda_2$  in the three-mode system. For simplicity, we set  $\kappa_2 = \kappa_3 = 0$ , and assume  $\kappa_1$  has a fixed nonzero value  $\kappa$ . At the three-fold degeneracy points  $\{\pm\lambda_1^c, \pm\lambda_2^c\}$ , the maximum gap among the three complex eigenenergies vanishes. Here the parameters  $\lambda_1$  and  $\lambda_2$  are scaled in unit of  $\kappa$ .  $\Delta_{n,m}$  denotes the difference between two eigenenergies, i.e.,  $E_n - E_m$  ( $n \neq m$ ,  $n, m = 1, 2, 3$ ). (d) The solid lines denote EP2s where a pair of eigenstates coalesce. Along the dashed lines, all the three eigenenergies have the same imaginary part. Their intersection points (red dots) are EP3s connecting Fermi arcs and i-Fermi arcs.

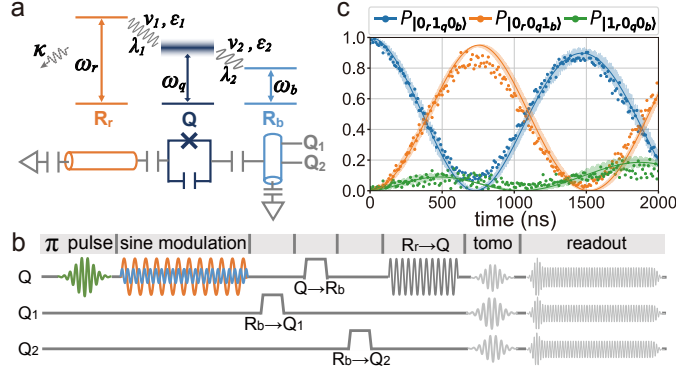


FIG. 2: Experimental implementation. (a) Synthesis of the NH three-mode system. The NH Hamiltonian is realized in a circuit, where a Josephson-junction-based qubit ( $Q$ ), together with a bus resonator ( $R_b$ ) and a readout resonator ( $R_r$ ), comprises an effective three-mode system in the single-excitation subspace. The decaying rates of  $Q$  and  $R_b$  are respectively 0.06 MHz and 0.08 MHz, both of which can be neglected compared to that of  $R_r$ ,  $\kappa = 5$  MHz.  $Q$  is coupled to  $R_r$  ( $R_b$ ) at the first upper (lower) sideband with respect to the first (second) parametric modulation. (b) Pulse sequence. The qubit  $Q$  is first prepared in the excited state at its idle frequency, followed by the application of two sine modulations. The modulation frequencies ( $\nu_1$ ,  $\nu_2$ ) and amplitudes are tunable for controlling  $\lambda_1$  and  $\lambda_2$ . After the modulating pulse, the evolved  $R_r$ - $Q$ - $R_b$  output state is mapped to the  $Q$ - $Q_2$ - $Q_1$  system for readout, where  $Q_1$  and  $Q_2$  are two ancilla qubits, each of which can be controllably coupled to the bus resonator. (c) Observed evolutions of the populations. All data are measured for the initial state  $|0_r 1_q 0_b\rangle$  at the point  $\lambda_1 = 2\pi \times 0.21$  MHz and  $\lambda_2 = 2\pi \times 0.31$  MHz. The results are obtained by discarding the measurement outcome  $|0_r 0_q 0_b\rangle$  and renormalizing the remaining populations of  $|0_r 0_q 1_b\rangle$ ,  $|0_r 1_q 0_b\rangle$ , and  $|1_r 0_q 0_b\rangle$  in the single-excitation subspace. The solid curves are theoretical predictions using the NH Hamiltonian (1), while the fast oscillating curves are numerical simulation results using the original Hamiltonian (given in Sec. S3 of the Supplemental material) with frequency modulations included.

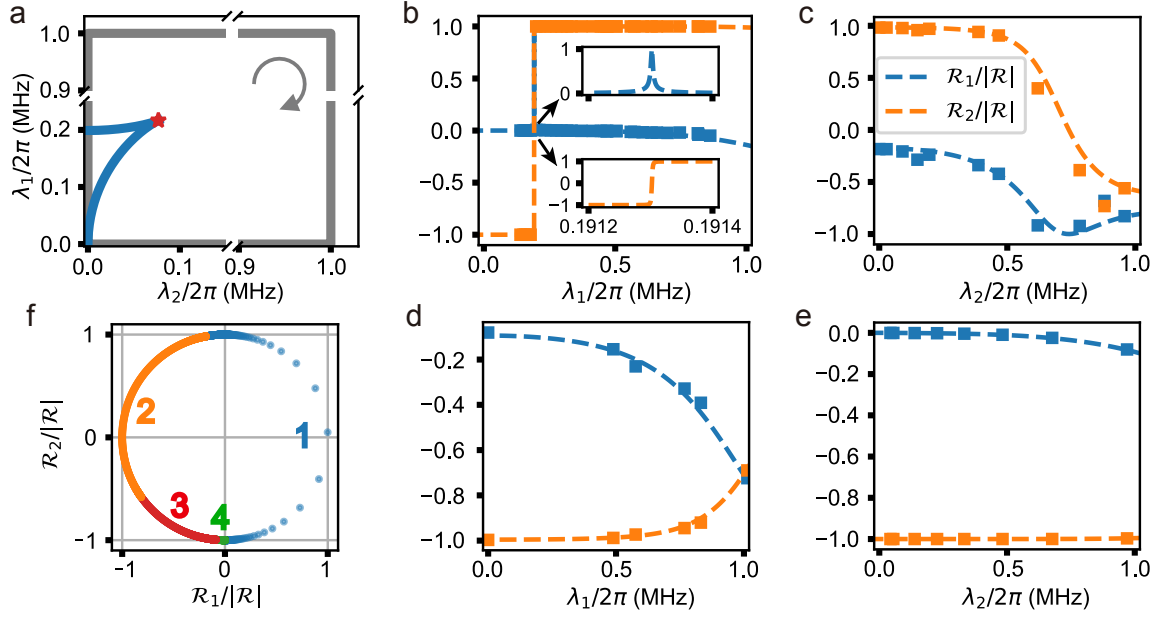


FIG. 3: Characterization of the NH topology. (a) Loop traversed for extracting the winding number. The loop (gray solid line) is square-shaped with four vertices  $(0,0)$ ,  $(\lambda_m, 0)$ ,  $(0, \lambda_m)$ , and  $(\lambda_m, \lambda_m)$ , where  $\lambda_m = 2\pi \times 1$  MHz. This loop surrounds an EP3 (red star), which connects two Fermi arcs consisting of EP2s (blue solid line). The arrow denotes the direction of the integral along the loop. (b)-(e) Normalized resultant vectors measured against  $\lambda_1$  with  $\lambda_2 = 0$  (b) and  $\lambda_m$  (d), and against  $\lambda_2$  with  $\lambda_1 = \lambda_m$  (c) and 0 (e). The squares represent the components  $\mathcal{R}_1/|\mathcal{R}|$  (blue) and  $\mathcal{R}_2/|\mathcal{R}|$  (orange), respectively. The dotted lines denote the fitted  $\mathcal{R}_1/|\mathcal{R}|$  and  $\mathcal{R}_2/|\mathcal{R}|$  as functions of  $\lambda_1$  or  $\lambda_2$ . The winding number, calculated with these fitted functions, is 1. (f) Trajectory of the rescaled unit resultant vector  $\mathcal{R}^u = (\mathcal{R}_1 + i\mathcal{R}_2)/|\mathcal{R}|$ . The symbols “1”, “2”, “3”, and “4”, label the sections associated with the four edges of the parameter-space loop, shown in (b), (c), (d), and (e), respectively.



# Supplementary Materials for “Measuring topological invariants for higher-order exceptional points in quantum three-mode systems”

Pei-Rong Han<sup>1,2</sup>, Wen Ning<sup>1</sup>, Xin-Jie Huang<sup>1</sup>, Ri-Hua Zheng<sup>1</sup>, Shou-Bang Yang<sup>1</sup>, Fan Wu<sup>1</sup>, Zhen-Biao Yang<sup>1,3,\*</sup>, Qi-Ping Su<sup>4</sup>, Chui-Ping Yang<sup>4,†</sup> and Shi-Biao Zheng<sup>1,3,‡</sup>

<sup>1</sup>*Fujian Key Laboratory of Quantum Information and Quantum Optics,*

*College of Physics and Information Engineering,*

*Fuzhou University, Fuzhou, China*

<sup>2</sup>*School of Physics and Mechanical and Electrical Engineering,*

*Longyan University, Longyan, China*

<sup>3</sup>*Hefei National Laboratory, Hefei, China*

<sup>4</sup>*School of Physics, Hangzhou Normal University, Hangzhou, China*

## Contents

<b>S1 . Eigenenergies and eigenstates of the NH three-mode system</b>	1
<b>S2 . Simulation of conditional dynamics in the isofrequency region</b>	3
<b>S3 . Synthesis of the NH model</b>	4
<b>S4 . State readout</b>	5
<b>S5 . Extraction of eigenenergies</b>	5
<b>S6 . Characterization of the nonclassicality</b>	9
<b>S7 . Derivation of the resultant vector</b>	9
<b>S8 . Extraction of the winding number</b>	10
<b>S9 . Winding numbers for DPs and EP2s</b>	11
<b>References</b>	13

## S1 . EIGENENERGIES AND EIGENSTATES OF THE NH THREE-MODE SYSTEM

The non-Hermitian (NH) model under consideration involves three modes with nearest-neighbor couplings. The first mode has a non-negligible dissipation rate  $\kappa$ , while dissipation rates of the other two modes are negligible. The system dynamics associated with the no-jump trajectory is governed by the NH Hamiltonian (hereafter setting  $\hbar = 1$ )

$$H = -\frac{1}{2}i\kappa a_1^\dagger a_1 + \left( \lambda_1 a_1^\dagger a_2 + \lambda_2 a_2^\dagger a_3 + \text{H.c.} \right), \quad (\text{S1})$$

where  $a_j^\dagger$  and  $a_j$  ( $j = 1, \dots, 3$ ) denote the creation and annihilation operators of the  $j$ th mode,  $\lambda_j$  is the coupling coefficient between the  $j$ th and  $(j + 1)$ th modes, and H.c. indicates the Hermitian conjugate.

---

\*E-mail: zbyang@fzu.edu.cn

†E-mail: yangcp@hznu.edu.cn

‡E-mail: t96034@fzu.edu.cn

In the single-excitation subspace  $\{|1_1 0_2 0_3\rangle, |0_1 1_2 0_3\rangle, |0_1 0_2 1_3\rangle\}$ ,  $H$  has three eigenenergies, given by

$$E_{1,2} = -\frac{i\kappa}{6} - \frac{1}{3} \left[ \left( -\frac{1}{2} \mp i\frac{\sqrt{3}}{2} \right) \frac{\xi}{\alpha} + \left( -\frac{1}{2} \pm i\frac{\sqrt{3}}{2} \right) \alpha \right], \quad (\text{S2})$$

and

$$E_3 = -\frac{i\kappa}{6} - \frac{1}{3} \left( \frac{\xi}{\alpha} + \alpha \right), \quad (\text{S3})$$

where

$$\begin{aligned} \xi &= 3\lambda_1^2 + 3\lambda_2^2 - \frac{\kappa^2}{4}, \\ \alpha &= \sqrt[3]{\eta + \sqrt{\eta^2 - \xi^3}}, \end{aligned} \quad (\text{S4})$$

and

$$\eta = -\frac{i\kappa}{4} \left( 18\lambda_2^2 - 9\lambda_1^2 + \frac{\kappa^2}{2} \right). \quad (\text{S5})$$

Figure S1(a) illustrates either  $\min |\text{Im}(E_n - E_m)|$  or  $\min ||E_n| - |E_m||$  versus  $\lambda_1$  and  $\lambda_2$  scaled in unit of  $\kappa$ . Outside the colored region,  $\min |\text{Im}(E_n - E_m)|$  and  $\min ||E_n| - |E_m||$  are both 0. Considering this in conjunction with Fig. 1b of the main text, it can be concluded that there are at least two eigenenergies with equal imaginary parts and opposite real parts. Therefore, outside this colored region, the eigenenergy can be expressed as

$$\begin{aligned} E_1 &= iI_1, \\ E_2 &= R + iI, \\ E_3 &= -R + iI, \end{aligned} \quad (\text{S6})$$

where  $R$ ,  $I$ , and  $I_1$  are real parameters. Figure S1(b) shows the minimum of the scaled gaps  $\min |E_n - E_m|/\kappa$  ( $n, m = 1$  to  $3$ ,  $n \neq m$ ) among three complex eigenenergies versus  $\lambda_1$  and  $\lambda_2$ . The curves with  $\min |E_n - E_m| = 0$  correspond to lines of EP2s, where two of the three eigenenergies coalesce. The corresponding eigenstates are

$$|\Phi_j\rangle = N_j \left\{ \left[ E_j \left( E_j + \frac{i\kappa}{2} \right) \right] |0_1 0_2 1_3\rangle + \lambda_2 \left( E_j + \frac{i\kappa}{2} \right) |0_1 1_2 0_3\rangle + \lambda_1 \lambda_2 |1_1 0_2 0_3\rangle \right\} \quad (j = 1, 2, 3), \quad (\text{S7})$$

where  $N_j$  is the normalization factor.

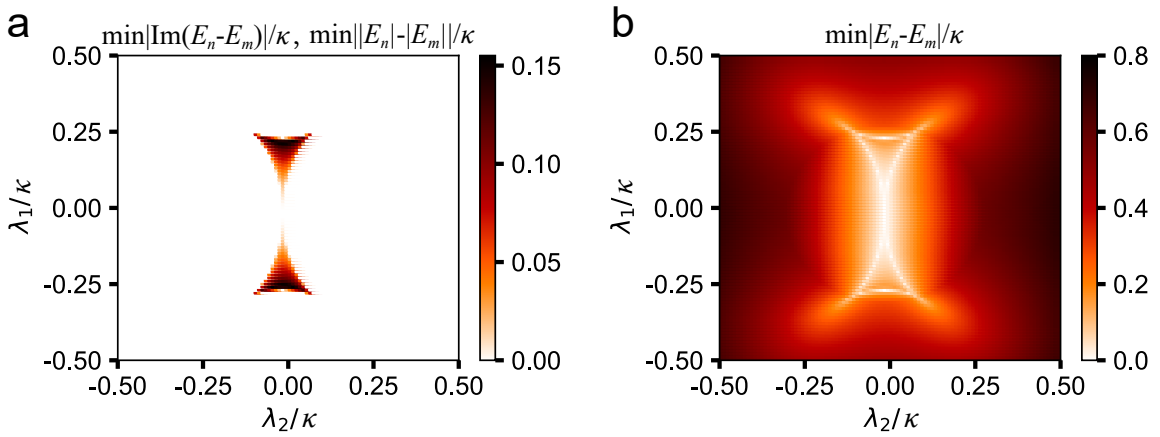


FIG. S1: Characterization of eigenenergies. (a) The colored region is complementary to Fig. 1b in the main text. Outside this region, there is  $\min |\text{Im}(E_n - E_m)| = \min ||E_n| - |E_m|| = 0$ , indicating that at least two eigenenergies have equal imaginary parts and opposite real parts. (b) The lines of 2EPs are highlighted, which corresponds to  $\min |E_n - E_m| = 0$ .

When  $\lambda_1 \neq 0$  and  $\lambda_2 \neq 0$ , each of these eigenstates is a tripartite entangled state, for which each mode is entangled with the other two modes. The system has four 3EPs at  $\{\pm\lambda_1^c, \pm\lambda_2^c\}$  with  $\lambda_1^c = \sqrt{2}\kappa/3\sqrt{3}$  and  $\lambda_2^c = \kappa/6\sqrt{3}$ . For the EP3 in the first quadrant, the three-fold degenerate eigenenergy is

$$E_{\text{EP3}} = -\frac{i\kappa}{6} \quad (\text{S8})$$

with the corresponding eigenstate

$$|\Phi_{\text{EP3}}\rangle = -\sqrt{\frac{1}{6}}|0_1 0_2 1_3\rangle + i\sqrt{\frac{1}{2}}|0_1 1_2 0_3\rangle + \sqrt{\frac{1}{3}}|1_1 0_2 0_3\rangle. \quad (\text{S9})$$

This three-fold degenerate eigenstate is a genuine tripartite entangled state, manifested by the non-zero pairwise concurrences  $\mathcal{C}_{1,2} = \sqrt{\frac{2}{3}}$ ,  $\mathcal{C}_{2,3} = \sqrt{\frac{1}{3}}$ , and  $\mathcal{C}_{1,3} = \sqrt{\frac{2}{9}}$ .

## S2 . SIMULATION OF CONDITIONAL DYNAMICS IN THE ISOFREQUENCY REGION

After some calculations, we find  $\eta^2 - \xi^3 > 0$  in the isofrequency region. Therefore, we can rewrite the parameter  $\alpha$  in Eq. S4 as

$$\alpha = (a + ib)^{1/3}, \quad (\text{S10})$$

where  $a = \sqrt{\eta^2 - \xi^3}$  and  $b = -i\eta$  are real numbers. With this expression, it is easy to check

$$\begin{aligned} |\alpha|^2 &= (a^2 + b^2)^{1/3} \\ &= -\left(3\lambda_1^2 + 3\lambda_2^2 - \frac{\kappa^2}{4}\right) \\ &= -\xi. \end{aligned} \quad (\text{S11})$$

Then, we obtain  $\xi/|\alpha|^2 = -1$ . By using  $1/\alpha = \alpha^*/|\alpha|^2$ , we can further obtain that  $\xi/\alpha = -\alpha^*$ . Substituting the result into Eq. S2 and Eq. S3, we have

$$E_{1,2} = -\frac{i\kappa}{6} - i\frac{1}{3} \left[ \pm\sqrt{3}\text{Re}(\alpha) - \text{Im}(\alpha) \right] \quad (\text{S12})$$

and

$$E_3 = -\frac{i\kappa}{6} - i\frac{2}{3}\text{Im}(\alpha). \quad (\text{S13})$$

Obviously, the result shows that real parts of three eigenenergies vanish in the isofrequency region. Figure S2 shows the simulated evolutions of corresponding eigenstates' fidelities, pairwise concurrences, and the probability for the no-jump trajectory of the initial state  $|0_1 0_2 1_3\rangle$  in the region with  $\lambda_1/\kappa = 0.2$  and  $\lambda_2/\kappa = 0.02$  by using the NH Hamiltonian of Eq. S1. In such a region each of the pairwise concurrences tends to a fixed value for the no-jump case at the price of a progressively decreasing probability.

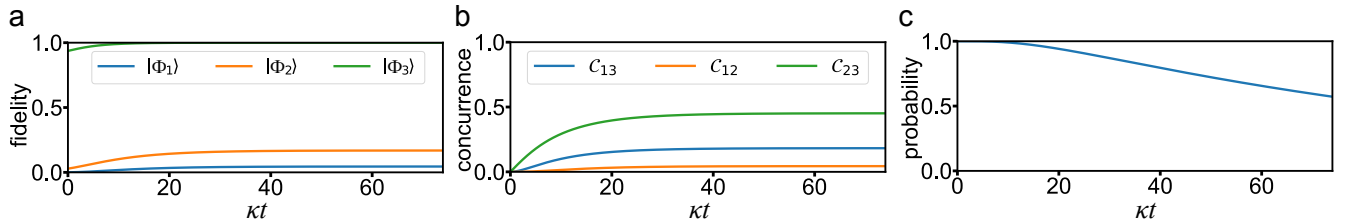


FIG. S2: The fidelity (a), concurrence (b) and probability (c) evolution for the no-jump trajectory of the initial state  $|0_1 0_2 1_3\rangle$  with  $\lambda_1/\kappa = 0.2$  and  $\lambda_2/\kappa = 0.02$ .  $|\Phi_1\rangle$ ,  $|\Phi_2\rangle$  and  $|\Phi_3\rangle$  are the three eigenstates for which the coefficients of the components  $|1_1 0_2 0_3\rangle$ ,  $|0_1 1_2 0_3\rangle$  and  $|0_1 0_2 1_3\rangle$  have a maximum modulus.

### S3 . SYNTHESIS OF THE NH MODEL

The experiment is performed in a circuit quantum electrodynamics architecture involving five frequency-tunable Xmon qubits, each individually coupled to a readout resonator, and all connected to a bus resonator ( $R_b$ ) with a fixed frequency  $\omega_b/2\pi = 5.58$  GHz, as sketched in Fig. S3. Every Xmon qubit used in our experiment has a microwave line (XY line) to drive its state transition and an individual flux line (Z line) to dynamically tune its frequency. The NH three-mode system is synthesized with the bus resonator, one of the Xmon qubits ( $Q$ ), and its readout resonator ( $R_r$ ) with a fixed frequency  $\omega_r/2\pi = 6.66$  GHz. The  $R_b$ - $Q$  and  $Q$ - $R_r$  swapping interactions are realized by applying two parametric modulations to  $Q$ , making its frequency depend on time as

$$\omega_q = \omega_0 + \varepsilon_1 \cos(\nu_1 t) + \varepsilon_2 \cos(\nu_2 t), \quad (\text{S14})$$

where  $\omega_0$  is the mean frequency, and  $\varepsilon_j$  and  $\nu_j$  ( $j = 1, 2$ ) are the corresponding modulation amplitude and angular frequency of the  $j$ th modulation, respectively. In the experiment,  $\varepsilon_j$  and  $\nu_j$  can be readily manipulated by a Z control line.

$Q$  is capacitively coupled to  $R_b$  and  $R_r$  (see Ref. [1] for details). The coherent Hamiltonian of the total system is given by

$$H = H_0 + H_I, \quad (\text{S15})$$

where

$$H_0 = \omega_b a_b^\dagger a_b + \omega_r a_r^\dagger a_r + \omega_q |e\rangle \langle e|, \quad (\text{S16})$$

and

$$H_I = |0_q\rangle \langle 1_q| \left( g_b a_b^\dagger + g_r a_r^\dagger \right) + \text{H.c.}, \quad (\text{S17})$$

where  $a_r^\dagger$  ( $a_b^\dagger$ ) and  $a_r$  ( $a_b$ ) denote the creation and annihilation operators for the photonic field stored in  $R_r$  ( $R_b$ ),  $|0_q\rangle$  and  $|1_q\rangle$  denote the ground and first excited states of  $Q$ , and  $g_b$  ( $g_r$ ) is the on-resonance  $R_b$ - $Q$  ( $Q$ - $R_r$ ) coupling strength.

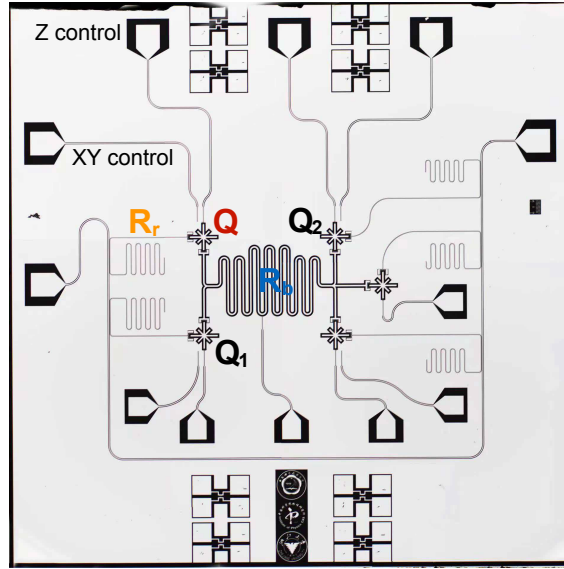


FIG. S3: Circuit micrograph.

Performing the transformation  $e^{i \int_0^t H_0 dt}$ , we obtain the system Hamiltonian in the interaction picture,

$$H'_I = e^{-i\mu_1 \sin(\nu_1 t)} e^{-i\mu_2 \sin(\nu_2 t)} |0_q\rangle \langle 1_q| \left( e^{i\delta_b t} g_b a_b^\dagger + e^{i\delta_r t} g_r a_r^\dagger \right) + \text{H.c.}, \quad (\text{S18})$$

where  $\mu_j = \varepsilon_j/\nu_j$  ( $j = 1, 2$ ),  $\delta_b = \omega_b - \omega_0$ , and  $\delta_r = \omega_r - \omega_0$ . Using the Jacobi-Anger expansion

$$e^{-i\mu_j \sin(\nu_j t)} = \sum_{n=-\infty}^{\infty} J_n(\mu_j) e^{-in\nu_j t}, \quad (\text{S19})$$

with  $J_n(\mu_j)$  being the  $n$ th Bessel function of the first kind,  $H'_I$  can be rewritten as

$$H'_I = \sum_{m,n=-\infty}^{\infty} J_m(\mu_1) J_n(\mu_2) e^{-im\nu_1 t} e^{-in\nu_2 t} |0_q\rangle \langle 1_q| \left( e^{i\delta_b t} g_b a_b^\dagger + e^{i\delta_r t} g_r a_r^\dagger \right) + \text{H.c.} \quad (\text{S20})$$

Under the conditions  $\nu_1 = \delta_r$  and  $\nu_2 = -\delta_b$ ,  $Q$  is resonantly coupled to  $R_r$  ( $R_b$ ) at the first upper (lower) sideband with respect to the first (second) modulation. When  $g_b, g_r \ll \nu_1, \nu_2$ , the fast-oscillating terms can be discarded, so that  $H'_I$  reduces to

$$H'_I = |0_q\rangle \langle 1_q| \left( \lambda_1 a_b^\dagger + \lambda_2 a_r^\dagger \right) + \text{H.c.}, \quad (\text{S21})$$

where  $\lambda_1 = g_r J_1(\mu_1) J_0(\mu_2)$  and  $\lambda_2 = g_b J_0(\mu_1) J_1(\mu_2)$ , as depicted in Fig. 2a of the main text. In the single-excitation subspace,  $a_b^\dagger$  and  $a_r^\dagger$  can be replaced by  $|1_b\rangle \langle 0_b|$  and  $|1_r\rangle \langle 0_r|$ , respectively. Then  $H'_I$  is equivalent to the Hermitian part of the Hamiltonian (1) of the main text with  $N = 3$ . In our system, the dissipation rates of  $R_b$  and  $Q$  are respectively 0.08 MHz and 0.06 MHz, which are negligible compared with that of  $R_r$ . With the dissipation being included, the NH Hamiltonian is given by Eq. S1, with  $R_r$ ,  $Q$ , and  $R_b$  corresponding to the first, second, and last qubits, respectively.

#### S4 . STATE READOUT

The readout of the output  $R_b$ - $Q$ - $R_r$  state is enabled with two ancilla qubits, denoted as  $Q_1$  and  $Q_2$ . After the NH Hamiltonian dynamics, the state of  $R_b$  is mapped to  $Q_1$  through a swapping gate, which is realized by tuning the transition frequency of  $Q_1$  to  $\omega_b$  for a duration  $t_{sw} = \pi/(2g_1) \simeq 12.3$  ns, with  $g_1 = 2\pi \times 20.3$  MHz being the  $R_b$ - $Q$  photonic swapping rate. Then, the state of  $Q$  is transferred to  $Q_2$  by subsequently performing the  $Q$ - $R_b$  and  $R_b$ - $Q_2$  swapping gates. Finally,  $R_r$ 's state is transferred to  $Q$ . As the maximum frequency of  $Q$  ( $2\pi \times 6.01$  GHz) is smaller than  $\omega_r$  by an amount much larger than  $g_r$ , it is necessary to use the parametric modulation to realize the  $R_r$ - $Q$  mapping. The corresponding gate duration is 150 ns. With a correction for the state distortion during the state mapping, the resulting  $Q_1$ - $Q_2$ - $Q$  output state corresponds to the  $R_b$ - $Q$ - $R_r$  output state right before the state mapping.

#### S5 . EXTRACTION OF EIGENENERGIES

In our experiment, we choose a square-shaped loop on the  $\lambda_1$ - $\lambda_2$  plane to extract the winding number. The four vertices of the rectangle are  $(0, 0)$ ,  $(\lambda_m, 0)$ ,  $(0, \lambda_m)$ , and  $(\lambda_m, \lambda_m)$  with  $\lambda_m \simeq 2\pi \times 1$  MHz. Along the edge with  $\lambda_1 = 0$ ,  $R_r$  is decoupled from the  $Q$ - $R_b$  subsystem. In the interaction picture, the  $Q$ - $R_b$  swapping coupling is described by the Hamiltonian

$$\mathcal{H} = \lambda_2 \left( a_b^\dagger |0_q\rangle \langle 1_q| + a_b |1_q\rangle \langle 0_q| \right), \quad (\text{S22})$$

where  $a_b^\dagger$  and  $a_b$  denote the creation and annihilation operators for the photonic mode stored in  $R_b$ , and  $|0_q\rangle$  and  $|1_q\rangle$  represent the ground and excited states of  $Q$ . In the single-excitation subspace, this Hamiltonian has two eigenenergies  $E_\pm = \pm \lambda_2$ . The corresponding eigenstates are

$$|\Phi_\pm\rangle = \frac{1}{\sqrt{2}} (|0_b 1_q\rangle \pm |1_b 0_q\rangle). \quad (\text{S23})$$

The subsystem, starting from the initial state  $|0_b 1_q\rangle$ , evolves as

$$\cos(\lambda_2 t) |0_b 1_q\rangle - i \sin(\lambda_2 t) |1_b 0_q\rangle. \quad (\text{S24})$$

The value of  $\lambda_2$ , which depends on the amplitude and frequency of the parametric modulation used to mediate the sideband interaction, is inferred from the observed Rabi oscillation. The population evolutions for the state  $|0_b 1_q\rangle$ ,



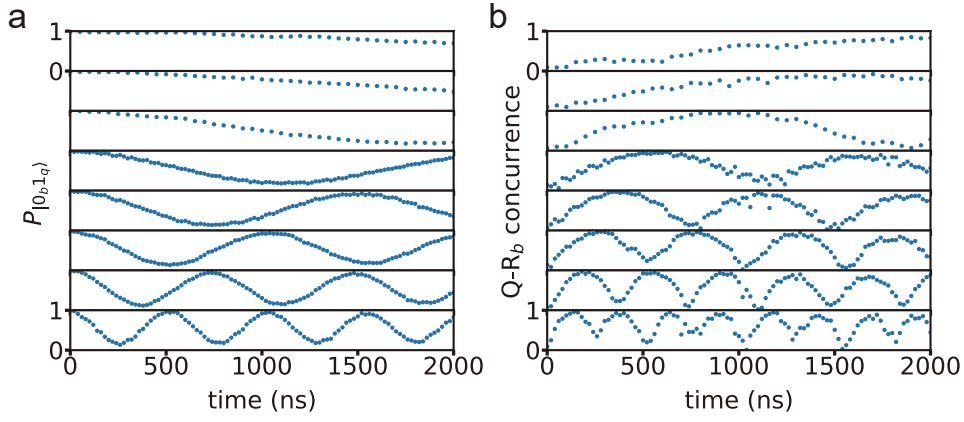


FIG. S4: The population (a) and concurrence (b) evolutions for different values of  $\lambda_2$  when  $\lambda_1 = 0$ , i.e., the edge from  $(0, 0)$  to  $(0, \lambda_m)$ . From top to bottom, the values of  $\lambda_2/2\pi$  are 0.04, 0.05, 0.14, 0.23, 0.33, 0.48, 0.68 and 0.97 MHz, respectively.

observed for different values of  $\lambda_2$ , are presented in Fig. S4(a). The  $Q-R_b$  concurrences associated with the two eigenstates  $|\Phi_{\pm}\rangle$ , extracted at  $\lambda_2 = \lambda_m$ , are 0.997 and 0.997, respectively.

For  $\lambda_2 = 0$ ,  $R_b$  is decoupled from the  $Q-R_r$  subsystem. In this case, the evolution of the  $Q-R_r$  subsystem associated with the no-jump trajectory is described by the NH Hamiltonian

$$\mathcal{H}' = \lambda_1 (a_r^\dagger |0_q\rangle \langle 1_q| + a_r |1_q\rangle \langle 0_q|) - \frac{i}{2} \kappa a_r^\dagger a_r, \quad (\text{S25})$$

where  $a_r^\dagger$  ( $a_r$ ) is the photonic creation (annihilation) operator for  $R_r$ . In the single-excitation subspace, the  $\mathcal{H}'$  has two eigenenergies

$$E'_\pm = -i\kappa/4 \pm \sqrt{\lambda_1^2 - \kappa^2/16}. \quad (\text{S26})$$

The corresponding eigenstates are

$$|\Phi'_\pm\rangle = \mathcal{N}_\pm \left( |1_q 0_r\rangle + \frac{E'_\pm}{\lambda_1} |0_q 1_r\rangle \right), \quad (\text{S27})$$

where  $\mathcal{N}_\pm = \left(1 + |E'_\pm/\lambda_1|^2\right)^{-1/2}$ . Fig. S5(a) shows the measured population of the state  $|1_q 0_r\rangle$  versus  $\lambda_1$  and  $t$ . This population is obtained by discarding the outcome  $|0_q 0_r\rangle$ , and then renormalizing the probabilities for the outcomes of  $|1_q 0_r\rangle$  and  $|0_q 1_r\rangle$ . The gap of the two eigenenergies versus  $\lambda_1$ , extracted from the population evolution, are shown in Fig. S5(c).

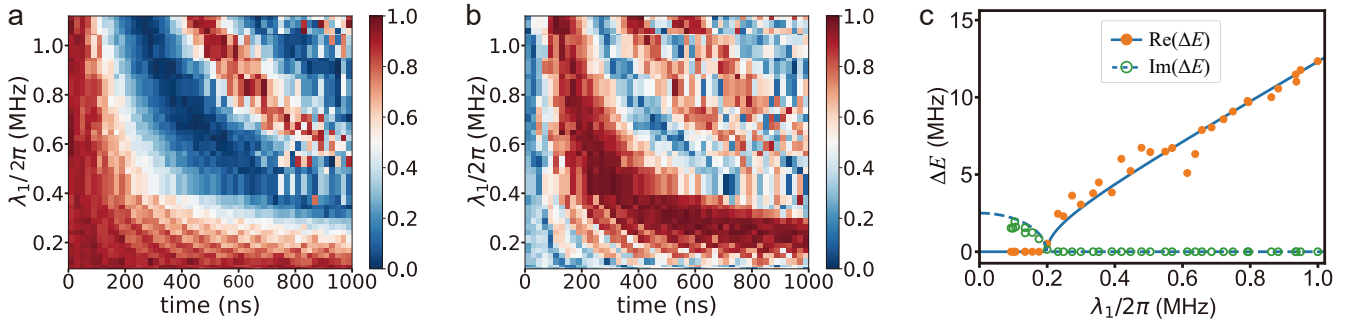


FIG. S5: The population (a) and concurrence (b) evolutions for different values of  $\lambda_1$  when  $\lambda_2 = 0$ , i.e., the edge from  $(0, 0)$  to  $(\lambda_m, 0)$ . (c) Spectral gap  $\Delta E$ . The solid and dashed lines denote the real and imaginary parts, respectively.

When  $\lambda_1 \neq 0$  and  $\lambda_2 \neq 0$ , the evolution of the  $R_b-Q-R_r$  system associated with the no-jump trajectory is governed by the Hamiltonian

$$\mathcal{H} = \mathcal{H}^H + \mathcal{H}^{NH}, \quad (\text{S28})$$

where

$$\begin{aligned} \mathcal{H}^H &= |1_q\rangle \langle 0_q| (\lambda_1 a_r + \lambda_2 a_b) + \text{H.c.}, \\ \mathcal{H}^{NH} &= -\frac{1}{2} i \kappa a_r^\dagger a_r. \end{aligned} \quad (\text{S29})$$

Suppose that the loop on the  $\lambda_1 - \lambda_2$  plane is a rectangle with four vertices  $(0, 0)$ ,  $(\lambda_m, 0)$ ,  $(0, \lambda_m)$ , and  $(\lambda_m, \lambda_m)$ . On the edges from  $(0, 0)$  to  $(\lambda_m, 0)$  and to  $(0, \lambda_m)$ , the system reduces to a two-mode system, so that the eigenspectra can be extracted relatively easily. Without dissipation, the three eigenstates of  $\mathcal{H}^H$  on the other two edges are given by

$$\begin{aligned} |\Phi_1\rangle &= \sin \theta |1_b 0_q 0_r\rangle - \cos \theta |0_b 0_q 1_r\rangle, \\ |\Phi_2\rangle &= \frac{1}{\sqrt{2}} (\cos \theta |1_b 0_q 0_r\rangle + \sin \theta |0_b 0_q 1_r\rangle + |0_b 1_q 0_r\rangle), \\ |\Phi_3\rangle &= \frac{1}{\sqrt{2}} (\cos \theta |1_b 0_q 0_r\rangle + \sin \theta |0_b 0_q 1_r\rangle - |0_b 1_q 0_r\rangle), \end{aligned} \quad (\text{S30})$$

where  $\tan \theta = \lambda_1 / \lambda_2$ . The corresponding eigenenergies are  $E_1^H = 0$  and  $E_2^H = -E_3^H = \lambda$ , with  $\lambda = \sqrt{\lambda_1^2 + \lambda_2^2}$ .

In the basis  $\{|\Phi_j\rangle\}$  ( $j = 1, 2, 3$ ),  $\mathcal{H}^{NH}$  can be expressed as

$$\mathcal{H}^{NH} = \mathcal{H}^{dg} + \mathcal{H}^{ndg}, \quad (\text{S31})$$

where  $\mathcal{H}^{dg}$  and  $\mathcal{H}^{ndg}$  represent the diagonal and off-diagonal parts respectively, given by

$$\mathcal{H}^{dg} = \begin{pmatrix} -i\frac{\kappa}{2} \cos^2 \theta & 0 & 0 \\ 0 & -i\frac{\kappa}{4} \sin^2 \theta & 0 \\ 0 & 0 & -i\frac{\kappa}{4} \sin^2 \theta \end{pmatrix}, \quad (\text{S32})$$

and

$$\mathcal{H}^{ndg} = \begin{pmatrix} 0 & i\frac{\kappa}{4\sqrt{2}} \sin(2\theta) & i\frac{\kappa}{4\sqrt{2}} \sin(2\theta) \\ i\frac{\kappa}{4\sqrt{2}} \sin(2\theta) & 0 & i\frac{\kappa}{4} \sin^2 \theta \\ i\frac{\kappa}{4\sqrt{2}} \sin(2\theta) & i\frac{\kappa}{4} \sin^2 \theta & 0 \end{pmatrix}. \quad (\text{S33})$$

In the basis  $\{|\Phi_j\rangle\}$ , we can rewrite the total Hamiltonian as

$$\mathcal{H} = \mathcal{H}^0 + \mathcal{H}^{ndg}, \quad (\text{S34})$$

where

$$\begin{aligned} \mathcal{H}^0 &= \mathcal{H}^H + \mathcal{H}^{dg} \\ &= \begin{pmatrix} -i\frac{\kappa}{2} \cos^2 \theta & 0 & 0 \\ 0 & \lambda - i\frac{\kappa}{4} \sin^2 \theta & 0 \\ 0 & 0 & -\lambda - i\frac{\kappa}{4} \sin^2 \theta \end{pmatrix}. \end{aligned} \quad (\text{S35})$$

We note  $\mathcal{H}^{ndg}$  can be treated as a perturbation, which is explained as follow. On the edge with  $\lambda_1 = \lambda_m$ ,  $\theta$  changes from  $\pi/2$  to  $\pi/4$ . For  $\theta = \pi/2$ , the non-zero off-diagonal elements are  $\mathcal{H}_{2,3}^{ndg}$  and  $\mathcal{H}_{3,2}^{ndg}$ , which have a magnitude of  $|\mathcal{H}_{2,3}^{ndg}| = \kappa/4$ . The ratio of this magnitude to the gap between the last two eigenvalues of  $\mathcal{H}^0$  is  $|\mathcal{H}_{2,3}^{ndg}| / |\mathcal{H}_{2,2}^0 - \mathcal{H}_{3,3}^0| = \kappa/8\lambda \simeq 0.099$ . When  $\theta$  changes to  $\pi/4$ ,  $|\mathcal{H}_{2,3}^{ndg}| / |\mathcal{H}_{2,2}^0 - \mathcal{H}_{3,3}^0|$  monotonously decreases to 0.070, while  $|\mathcal{H}_{1,2}^{ndg}| / |\mathcal{H}_{1,1}^0 - \mathcal{H}_{2,2}^0|$  approximately increases to  $\kappa/(4\sqrt{2}\lambda) \simeq 0.099$ . On the edge with  $\lambda_2 = \lambda_m$ ,  $\theta$  changes from 0 to  $\pi/4$ . For  $\theta = 0$ , all the off-diagonal elements are 0. When  $\theta$  increases to  $\pi/4$ ,  $|\mathcal{H}_{1,2}^{ndg}| / |\mathcal{H}_{1,1}^0 - \mathcal{H}_{2,2}^0|$

and  $|\mathcal{H}_{2,3}^{ndg}|/|\mathcal{H}_{2,2}^0 - \mathcal{H}_{3,3}^0|$  approximately increase to 0.098 and 0.099, respectively. These results imply that the magnitude of each off-diagonal element is much smaller than the corresponding energy gap, which ensures the perturbation condition. To the first order correction, the three eigenenergies correspond to the diagonal elements of  $\mathcal{H}^0$ . This indicates that the real part of the first eigenenergy  $E_1$  is approximately zero, and the other two eigenenergies  $E_2$  and  $E_3$  have the same imaginary part but opposite real parts. Therefore, the three eigenenergies can be approximately expressed as

$$\begin{aligned} E_1 &\simeq -iI_1, \\ E_2 &\simeq R - iI_2, \\ E_3 &\simeq -R - iI_2, \end{aligned} \quad (\text{S36})$$

where  $R$ ,  $I_1$ , and  $I_2$  are real parameters, with  $I_1 = \frac{\kappa}{2} \cos^2 \theta$  and  $I_2 = \frac{\kappa}{4} \sin^2 \theta$ . Consequently, the eigenenergies are determined by these three parameters  $\{R, I_1, I_2\}$ , which can be extracted through observation of the population evolutions.

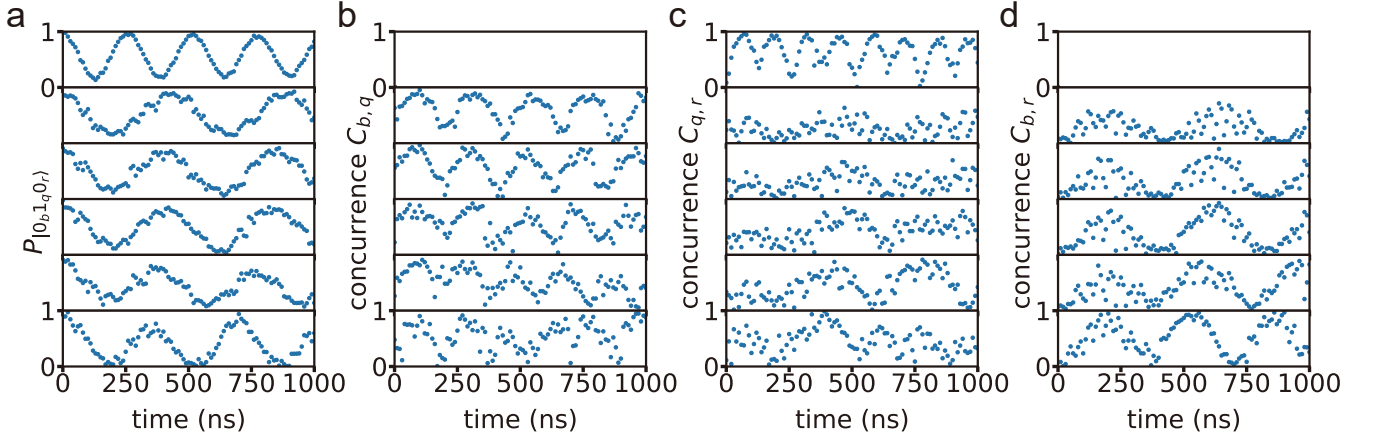


FIG. S6: The population (a) and concurrence (b),(c),(d) evolutions for different values of  $\lambda_1$  when  $\lambda_2 = \lambda_m$ , i.e., the edge from  $(0, \lambda_m)$  to  $(\lambda_m, \lambda_m)$ . From top to bottom, the values of  $\lambda_1/2\pi$  are 0, 0.49, 0.58, 0.77, 0.83 and 1.01 MHz, respectively.

Figure S6(a) displays the measured population of the state  $|0_b 1_q 0_r\rangle$  versus  $\lambda_1$  and  $t$  for the edge with  $\lambda_2 = \lambda_m$ . This population is obtained by discarding the outcome  $|0_b 0_q 0_r\rangle$ , and then renormalizing the probabilities of the three single-excitation outcomes. The eigenenergies in terms of  $R$  and  $\Delta I$  ( $= |I_1 - I_2|$ ) versus  $\lambda_1$ , extracted from this population evolution, are displayed in Fig. S7(a). Figure S10(a) shows the measured  $|0_b 1_q 0_r\rangle$ -state population versus  $\lambda_2$  and  $t$  for the edge with  $\lambda_1 = \lambda_m$ . The extracted eigenenergies in terms of  $R$  and  $\Delta I$  versus  $\lambda_2$  are displayed in Fig. S7(b).

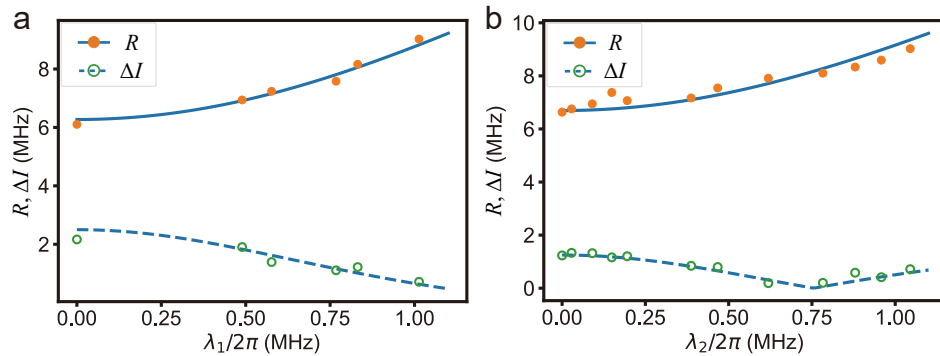


FIG. S7: The extracted eigenenergies in terms of  $R$  and  $\Delta I$  versus (a)  $\lambda_1$  and (b)  $\lambda_2$ .

## S6 . CHARACTERIZATION OF THE NONCLASSICALITY

Along the edge with  $\lambda_1 = 0$ ,  $R_r$  remains in the ground state  $|0_r\rangle$ . The measured  $Q$ - $R_b$  concurrence, versus  $\lambda_2$  and  $t$ , is displayed in Fig. S4(b). The density matrices for the two eigenstates  $|\Phi_{\pm}\rangle$ , extracted from the data measured at  $\lambda_2 = \lambda_m$ , are presented in Fig. S8. The concurrences corresponding to these two eigenstates are 0.997 and 0.997, respectively. Fig. S5(b) shows the  $Q$ - $R_r$  concurrence versus  $\lambda_1$  and  $t$ , measured for the edge  $\lambda_2 = 0$ . The measured density matrices, associated with the two eigenstates  $|\Phi'_{\pm}\rangle$  for  $\lambda_1 = \lambda_m$ , are presented in Fig. S9, with the concurrences 0.971 and 0.971.

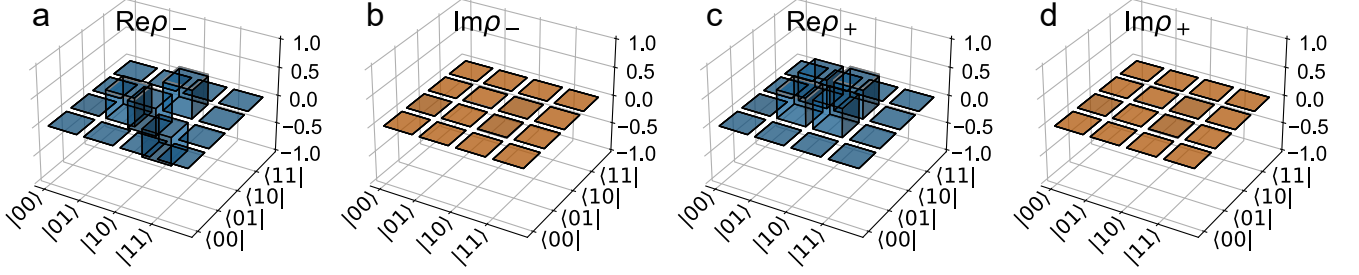


FIG. S8: The density matrices  $\rho_{\pm}$  for the two eigenstates  $|\Phi_{\pm}\rangle$ . (a) The real parts of  $\rho_{-}$ . (b) The imaginary parts of  $\rho_{-}$ . (c) The real parts of  $\rho_{+}$ . (d) The imaginary parts of  $\rho_{+}$ . The two numbers in each ket denote the excitation numbers of the qubit and the bus resonator, respectively. The black frames denote the matrix elements of the ideal eigenstates.

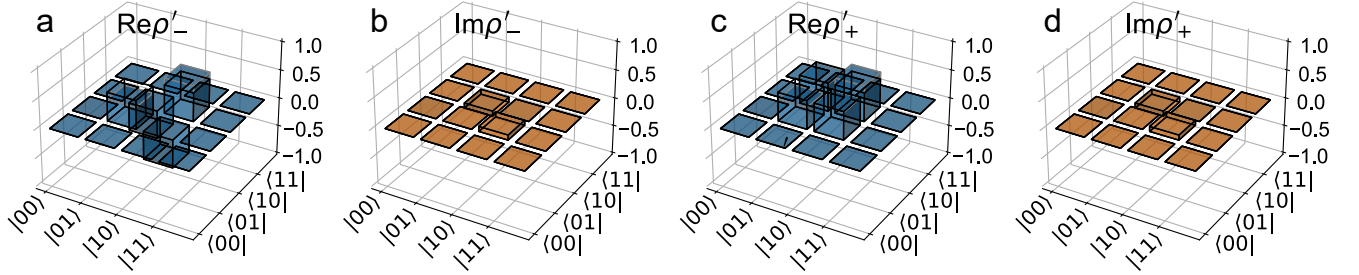


FIG. S9: The density matrices  $\rho'_{\pm}$  for the two eigenstates  $|\Phi'_{\pm}\rangle$ . (a) The real parts of  $\rho'_{-}$ . (b) The imaginary parts of  $\rho'_{-}$ . (c) The real parts of  $\rho'_{+}$ . (d) The imaginary parts of  $\rho'_{+}$ . The two numbers in each ket denote the excitation numbers of the qubit and the readout resonator, respectively. The black frames denote the matrix elements of the ideal eigenstates.

Figures S6(b), (c), and (d) present the measured three pairwise concurrences  $C_{b,q}$ ,  $C_{q,r}$ , and  $C_{b,r}$  versus  $\lambda_1$  and  $t$  for the edge with  $\lambda_2 = \lambda_m$ , where the subscript “b”, “q”, and “r” denote the bus resonator, Xmon qubit, and readout resonator, respectively. Figure S10(b), (c), and (d) showcase the three pairwise concurrences versus  $\lambda_2$  and  $t$  for the edge with  $\lambda_1 = \lambda_m$ . These results show that the tripartite system evolves from the initial product state  $|0_b 1_q 0_r\rangle$  to a tripartite entangled state under the NH Hamiltonian when  $\lambda_1 \neq 0$  and  $\lambda_2 \neq 0$ . For example, the three concurrences, measured at the point with  $\lambda_1 = \lambda_2 = \lambda_m$  for the time 600 ns, are  $C_{b,q} = 0.50$ ,  $C_{q,r} = 0.64$ , and  $C_{b,r} = 0.74$ , respectively. These results imply that the corresponding eigenstates are highly-nonclassical states, featuring tripartite quantum entanglement.

## S7 . DERIVATION OF THE RESULTANT VECTOR

The resultant is a basic concept in algebra. It can be used to determine whether two polynomials have common roots, defined as

$$R_{P_1, P_2} \equiv \det S_{P_1, P_2}, \quad (\text{S37})$$

where  $P_1$ ,  $P_2$  are two polynomials and  $S_{P_1, P_2}$  is their Sylvester matrix. Suppose

$$\begin{aligned} P_1 &= a_0 x^n + a_1 x^{n-1} + \dots + a_n, \\ P_2 &= b_0 x^m + b_1 x^{m-1} + \dots + b_m, \end{aligned} \quad (\text{S38})$$

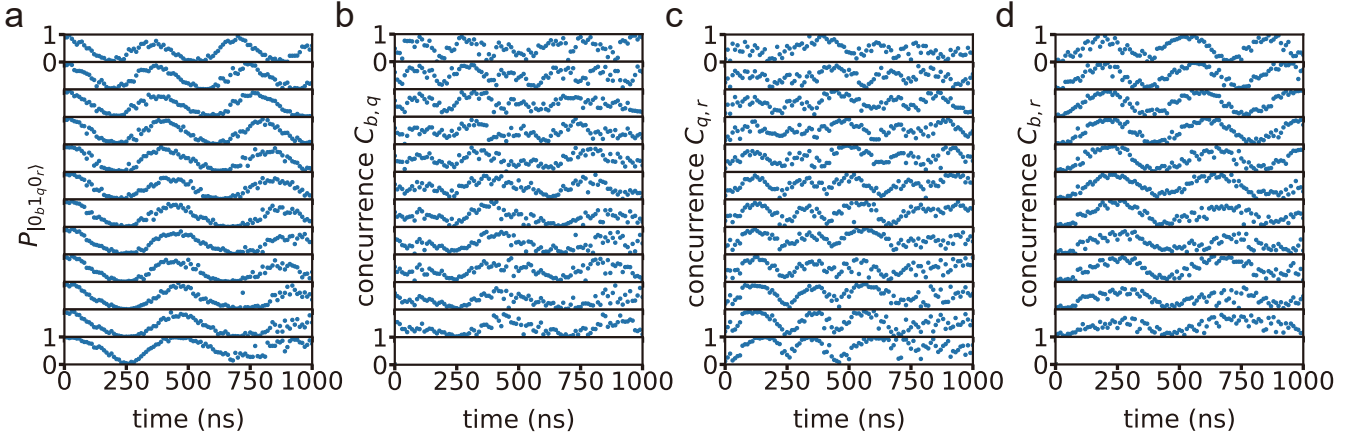


FIG. S10: The population (a) and concurrence (b),(c),(d) evolutions for different values of  $\lambda_2$  when  $\lambda_1 = \lambda_m$ , i.e., the edge from  $(\lambda_m, 0)$  to  $(\lambda_m, \lambda_m)$ . From top to bottom, the values of  $\lambda_2/2\pi$  are 1.04, 0.96, 0.88, 0.78, 0.62, 0.47, 0.39, 0.20, 0.15, 0.09, 0.03 and 0 MHz, respectively.

the corresponding resultant is a determinant of order  $m + n$ ,

$$R_{P_1, P_2} = \begin{vmatrix} a_0 & a_1 & a_2 & \dots & \dots & a_n & 0 & \dots & 0 \\ 0 & a_0 & a_1 & \dots & \dots & a_{n-1} & a_n & \dots & 0 \\ \vdots & \vdots & \vdots & \vdots & \vdots & \vdots & \vdots & \vdots & \vdots \\ 0 & 0 & \dots & 0 & a_0 & \dots & \dots & \dots & a_n \\ b_0 & b_1 & b_2 & \dots & \dots & \dots & b_m & \dots & 0 \\ 0 & b_0 & b_1 & \dots & \dots & \dots & b_{m-1} & b_m & \dots \\ \vdots & \vdots & \vdots & \vdots & \vdots & \vdots & \vdots & \vdots & \vdots \\ 0 & \dots & 0 & b_0 & b_1 & \dots & \dots & \dots & b_m \end{vmatrix}. \quad (\text{S39})$$

If  $R_{P_1, P_2} = 0$ , the polynomials  $P_1$  and  $P_2$  have common roots.

For a three-dimensional system governed by the Hamiltonian  $H$ , the characteristic polynomial  $P$  is given by

$$P = -(E - E_1)(E - E_2)(E - E_3), \quad (\text{S40})$$

where  $E_1$ ,  $E_2$  and  $E_3$  are the three eigenvalues of  $H$ . The first- and second-order derivatives of  $P(E)$  are

$$P' = -[(E - E_1)(E - E_2) + (E - E_2)(E - E_3) + (E - E_3)(E - E_1)], \quad (\text{S41})$$

and

$$P'' = -2[(E - E_1) + (E - E_2) + (E - E_3)]. \quad (\text{S42})$$

The two components of the resultant vector are given by

$$\mathcal{R}_1 = -R_{P, P'} = (E_1 - E_2)^2(E_1 - E_3)^2(E_2 - E_3)^2 \quad (\text{S43})$$

and

$$\mathcal{R}_2 = iR_{P, P''} = 8(E_1 + E_3 - 2E_2)(E_1 + E_2 - 2E_3)(E_2 + E_3 - 2E_1). \quad (\text{S44})$$

Therefore, we can calculate  $\mathcal{R}_1$  and  $\mathcal{R}_2$  at each point  $(\lambda_1, \lambda_2)$  of the parameter space with the measured eigenenergies. The results are presented in Fig. 3 of the main text.

## S8 . EXTRACTION OF THE WINDING NUMBER

The winding number, associated with each EP3, is calculated along a loop enclosing the EP3,

$$\mathcal{W} = \frac{1}{2\pi} \sum_{j=1,2} \oint_{C_\lambda} F(\mathcal{R}_1, \mathcal{R}_2) d\lambda_j, \quad (\text{S45})$$



where the integrand is given by

$$F(\mathcal{R}_1, \mathcal{R}_2) = \frac{1}{\|\mathcal{R}\|^2} \left( \mathcal{R}_1 \frac{\partial \mathcal{R}_2}{\partial \lambda_j} - \mathcal{R}_2 \frac{\partial \mathcal{R}_1}{\partial \lambda_j} \right). \quad (\text{S46})$$

The square-shaped loop chosen in our experiment encloses the EP3 in the first quadrant. Only one control parameter changes along each edge of the loop. Thus the integral can be rewritten as

$$\begin{aligned} \mathcal{W} = & \frac{1}{2\pi} \int_0^{\lambda_m} F(\mathcal{R}_1, \mathcal{R}_2) d\lambda_1 |_{\lambda_2=0} \\ & + \frac{1}{2\pi} \int_0^{\lambda_m} F(\mathcal{R}_1, \mathcal{R}_2) d\lambda_2 |_{\lambda_1=\lambda_m} \\ & + \frac{1}{2\pi} \int_{\lambda_m}^0 F(\mathcal{R}_1, \mathcal{R}_2) d\lambda_1 |_{\lambda_2=\lambda_m} \\ & + \frac{1}{2\pi} \int_{\lambda_m}^0 F(\mathcal{R}_1, \mathcal{R}_2) d\lambda_2 |_{\lambda_1=0}, \end{aligned} \quad (\text{S47})$$

where  $F(\mathcal{R}_1, \mathcal{R}_2)$  along the four edges are displayed in Fig. S11.

For simplicity, the square-shaped trajectory can be represented by the parametric equation

$$\begin{aligned} \lambda_1 &= \frac{1}{2} (1 - \cos \theta |\cos \theta| + \sin \theta |\sin \theta|), \\ \lambda_2 &= \frac{1}{2} (1 - \cos \theta |\cos \theta| - \sin \theta |\sin \theta|), \end{aligned} \quad (\text{S48})$$

where  $\theta$  ranges from 0 to  $2\pi$ . In this case, the winding number in terms of  $\theta$  is given by

$$\mathcal{W} = \frac{1}{2\pi} \int_0^{2\pi} \frac{1}{\|\mathcal{R}\|^2} \left( \mathcal{R}_1 \frac{\partial \mathcal{R}_2}{\partial \theta} - \mathcal{R}_2 \frac{\partial \mathcal{R}_1}{\partial \theta} \right) d\theta. \quad (\text{S49})$$

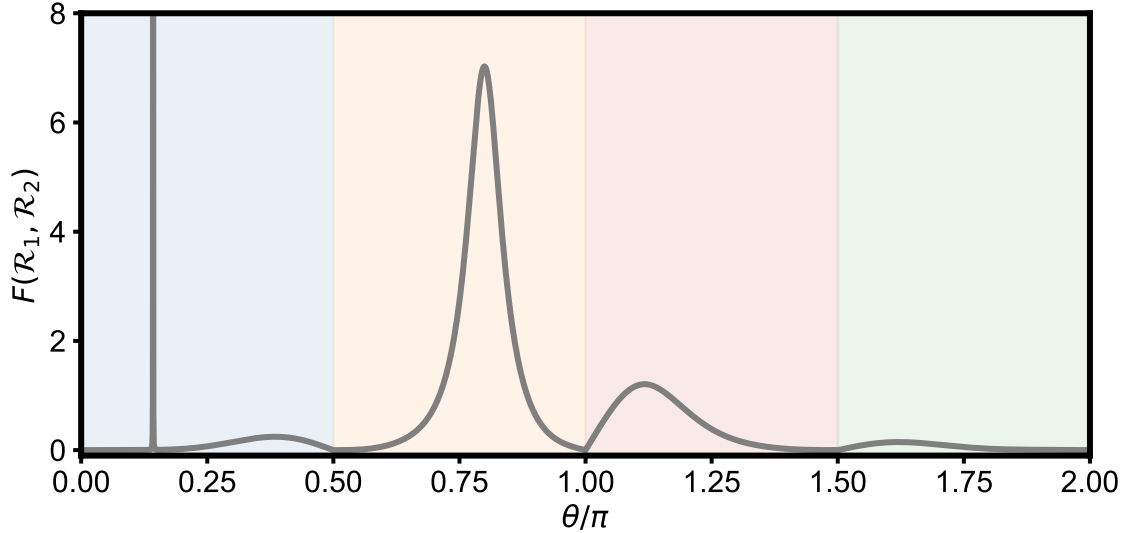


FIG. S11:  $F(\mathcal{R}_1, \mathcal{R}_2)$  along the four edges. Areas with different background colors correspond to the four edges.

## S9 . WINDING NUMBERS FOR DPS AND EP2S

To confirm that the winding number, defined by Eq.3 of the main text, is indeed uniquely associated with the topology for the three-order EPs, we here calculate this quantity for the DPs (diabolical points) in both the two-dimensional (2D) and 3D Hermitian system, as well as for the EP2s in a 2D NH system.

We first consider the 2D Hermitian system with the Hamiltonian  $H = \omega_x \sigma_x + \omega_y \sigma_y$ , where  $\omega_x$  ( $\omega_y$ ) is a real number. This model admits two real eigenenergies, and one could study the DP at  $\omega_x = \omega_y = 0$ . The characteristic polynomial of  $H$  is

$$P(E) = E^2 - (\omega_x^2 + \omega_y^2), \quad (\text{S50})$$

and its first-order derivative is

$$P'(E) = 2E. \quad (\text{S51})$$

The second-order derivative of  $P(E)$  is a constant,  $P''(E) = 2$ . In order to construct the Sylvester matrix of  $P(E)$  and  $P''(E)$ , we can take  $P''(E)$  as a polynomial of degree 1 with a zero coefficient,

$$P''(E) = 2 + 0E. \quad (\text{S52})$$

In this way, we have

$$S_{P,P'} = \begin{pmatrix} 1 & 0 & -(\omega_x^2 + \omega_y^2) \\ 2 & 0 & 0 \\ 0 & 2 & 0 \end{pmatrix} \text{ and } S_{P,P''} = \begin{pmatrix} 1 & 0 & -(\omega_x^2 + \omega_y^2) \\ 0 & 2 & 0 \\ 0 & 0 & 2 \end{pmatrix}. \quad (\text{S53})$$

The corresponding resultant  $\mathcal{R}_1 = R_{P,P'} \equiv \det S_{P,P'} = 1 - 4(\omega_x^2 + \omega_y^2)$  is a real-valued function, while  $\mathcal{R}_2 = R_{P,P''} \equiv \det S_{P,P''} = 4$  is a constant. Therefore, along a closed loop around DP in a 2D space spanned by  $\omega_x$  and  $\omega_y$ , the trajectory of resultant vector  $\mathcal{R}$  in the  $\mathcal{R}_1 - \mathcal{R}_2$  plane is a line segment instead of a closed curve, which means the winding number is always 0. We further note that the spectrum of any 2D Hermitian system has a similar structure, so that the corresponding winding number is zero.

We now turn to the 3D Hermitian system, whose dynamics is described by the three-mode Hamiltonian of Eq. S1 with  $\kappa = 0$ . In the single-excitation subspace, the Hamiltonian takes the form

$$H = \begin{pmatrix} 0 & \lambda_2 & 0 \\ \lambda_2 & 0 & \lambda_1 \\ 0 & \lambda_1 & 0 \end{pmatrix}, \quad (\text{S54})$$

with a DP at  $\lambda_1 = \lambda_2 = 0$ . The characteristic polynomial reads

$$P(E) = -E^3 + (\lambda_1^2 + \lambda_2^2)E \quad (\text{S55})$$

and its derivatives are

$$P'(E) = -3E^2 + (\lambda_1^2 + \lambda_2^2), \quad (\text{S56})$$

$$P''(E) = -6E. \quad (\text{S57})$$

We then have

$$S_{P,P'} = \begin{pmatrix} -1 & 0 & \lambda_1^2 + \lambda_2^2 & 0 & 0 \\ 0 & -1 & 0 & \lambda_1^2 + \lambda_2^2 & 0 \\ -3 & 0 & \lambda_1^2 + \lambda_2^2 & 0 & 0 \\ 0 & -3 & 0 & \lambda_1^2 + \lambda_2^2 & 0 \\ 0 & 0 & -3 & 0 & \lambda_1^2 + \lambda_2^2 \end{pmatrix} \quad (\text{S58})$$

and

$$S_{P,P''} = \begin{pmatrix} -1 & 0 & \lambda_1^2 + \lambda_2^2 & 0 \\ -6 & 0 & 0 & 0 \\ 0 & -6 & 0 & 0 \\ 0 & 0 & -6 & 0 \end{pmatrix}. \quad (\text{S59})$$

The corresponding resultants are

$$\begin{aligned} \mathcal{R}_1 &= R_{P,P'} \equiv \det S_{P,P'} \\ &= 4\lambda_2^6 + 12\lambda_2^4\lambda_1^2 + 12\lambda_2^2\lambda_1^4 + 4\lambda_1^6 \end{aligned} \quad (\text{S60})$$

and

$$\begin{aligned}\mathcal{R}_2 &= R_{P,P''} \equiv \det S_{P,P''} \\ &= 0.\end{aligned}\tag{S61}$$

Similar to *Example 1*,  $\mathcal{R}_1$  is a real-valued function, while  $\mathcal{R}_2$  is a constant. Therefore, we reach the same conclusion: the winding number defined by Eq.3 of the main text for the third-order DP is 0.

Finally, we consider the 2D dissipative system, with the NH Hamiltonian

$$H = \begin{pmatrix} 0 & J_x - iJ_y \\ J_x + iJ_y & -i\gamma/2 \end{pmatrix},\tag{S62}$$

where  $\gamma$  is the dissipation rate and  $|J| = \sqrt{J_x^2 + J_y^2}$  is the coupling strength. This Hamiltonian has two EP2s at  $J = \pm\gamma/4$ . The characteristic polynomial is

$$P(E) = E^2 + i\gamma/2E - |J|^2,\tag{S63}$$

and its derivatives read

$$P'(E) = 2E + i\gamma/2,\tag{S64}$$

$$P''(E) = 2.\tag{S65}$$

From this, we can obtain the Sylvester matrices

$$S_{P,P'} = \begin{pmatrix} 1 & i\frac{\gamma}{2} & -|J|^2 \\ 2 & i\frac{\gamma}{2} & 0 \\ 0 & 2 & i\frac{\gamma}{2} \end{pmatrix} \text{ and } S_{P,P''} = \begin{pmatrix} 1 & i\frac{\gamma}{2} & -|J|^2 \\ 0 & 2 & 0 \\ 0 & 0 & 2 \end{pmatrix}.\tag{S66}$$

Subsequently, two components of the resultant vector  $\mathcal{R}$  are given by

$$\mathcal{R}_1 = \gamma^2/4 - 4|J|^2,\tag{S67}$$

and

$$\mathcal{R}_2 = 4.\tag{S68}$$

Consistent with *Example 1* and *2*,  $\mathcal{R}_1$  is a real-valued function, while  $\mathcal{R}_2$  is a constant. As a result, along a closed loop around each EP2 in the  $J_x - J_y$  parameter space, the corresponding winding number of  $\mathcal{R}$  is 0.

These results confirm the claim of Ref. 12 of the main text that thus-defined winding number serves as a homotopy invariant, which uniquely characterizes the topology of EP3s.

- 
- [1] C. Song, S.-B. Zheng, P. Zhang, K. Xu, L. Zhang, Q. Guo, W. Liu, Da Xu, H. Deng, K. Huang, D. Zheng, X. Zhu, and H. Wang, Continuous-variable geometric phase and its manipulation for quantum computation in a superconducting circuit, *Nat. Commun.* **8**, 1061 (2017).